

On the Edge: the relation between stellar and dark matter haloes of Milky Way-mass galaxies

A. Genina^{1*}, A. J. Deason^{2,3} and C. S. Frenk²

¹ *Max-Planck-Institut für Astrophysik, Karl-Schwarzschild-Str. 1, D-85748, Garching, Germany*

² *Institute for Computational Cosmology, Department of Physics, Durham University, South Road, Durham DH1 3LE, UK*

³ *Centre for Extragalactic Astronomy, Department of Physics, Durham University, South Road, Durham DH1 3LE, UK*

Accepted XXX. Received YYY; in original form ZZZ

ABSTRACT

We investigate the build-up of the accreted stellar and dark matter haloes of Milky Way-like galaxies in APOSTLE suite of cosmological hydrodynamics simulations. We show that the stellar halo is made up primarily of stars stripped from a small number of massive dwarfs, most of which are disrupted by the present day. The dark matter halo, on the other hand, is made up primarily of small unresolved subhaloes ($\lesssim 10^6 M_{\odot}$) and a “smooth” component consisting of particles which were never bound to a subhalo. Despite these differences, the massive dwarfs that make up the majority of the stellar halo also contribute a significant fraction of the dark matter. The stars and dark matter stripped from these dwarfs are related through their kinematics and this leaves imprints in the phase-space structure of the haloes. We examine the relation between the location of features, such as caustics, in the phase space of the stars and dark halo properties. We show that the “edge” of the stellar halo is a probe of dark matter halo mass and assembly history. The edges of Milky Way-mass galaxies should be visible at a surface brightness of 31–36 mag arcsec⁻².

Key words: Galaxy: halo – Galaxy: formation – dark matter

1 INTRODUCTION

Within the Cold Dark Matter (CDM) model, structures form hierarchically, with small haloes forming first and merging to assemble larger objects (Davis et al. 1985). In the early Universe, some of the haloes have potential wells deep enough to allow the gas to become cool and dense, resulting in the formation of the first stars. Smaller haloes, with shallower potential wells may remain completely dark. The formation of stars triggers the reionization of hydrogen and helium atoms. The emitted radiation heats the halo gas above the virial temperature, bringing star formation to a halt in small haloes. More massive haloes will be able to maintain or re-accrete gas and continue star formation over long periods of time (Efstathiou 1992; Thoul & Weinberg 1996; Bullock et al. 2000; Benson et al. 2002; Benitez-Llambay & Frenk 2020). These haloes host bright galaxies that we can observe today.

The process of hierarchical structure formation leads to the build-up of the stellar and dark matter haloes of galaxies (Frenk et al. 1985). The dark matter halo of our own Galaxy, the Milky Way, is thus predicted to consist of its primordial dark matter component from the initial peak collapse, smoothly accreted dark matter and the dark matter that came from minor and major mergers with smaller haloes, some of which have hosted stars (Eggen et al. 1962; Searle & Zinn 1978; White & Rees 1978; Wang et al. 2011) that now make

up the stellar halo (Perek 1951; Roman 1954). Stellar haloes have also been identified in our nearest neighbour Andromeda (Mould & Kristian 1986; Pritchet & van den Bergh 1987) and beyond the Local Group (Davidge & Pritchet 1990; Minniti & Zijlstra 1996; Minniti et al. 1999; Harris & Harris 2000; Sarajedini et al. 2006; Chapman et al. 2006; Ibata et al. 2007a; Durrell et al. 2010; Monachesi et al. 2013; Harmsen et al. 2017).

The majority of the Milky Way’s stars belong to its disk component and the bar (Licquia & Newman 2015); however a non-negligible fraction resides in the Milky Way’s extended stellar halo. Within the CDM paradigm, these halo stars are the result of tidal stripping of infalling dwarf galaxies. Some fraction of halo stars could also have come from the heating of the stellar disk stars by supernovae feedback or molecular clouds, or from encounters with dwarf galaxies (Benson et al. 2004; Zolotov et al. 2009; Font et al. 2011; Yu et al. 2020; Gómez et al. 2017). A fraction of the stellar halo mass also stems from accreted globular clusters (Searle & Zinn 1978), some of which can be observed in the process of disruption today (Odenkirchen et al. 2001; Mateu et al. 2018; Starkman et al. 2020; Piatti & Carballo-Bello 2020). In this work, we exclusively consider the build up of the stellar haloes due to accretion. The Sagittarius dwarf galaxy (Ibata et al. 1994, 1995) and its extended tidal tails (Majewski et al. 2003) are an example of this process happening at the present day. Past mergers experienced by the Milky Way are expected to have left an imprint in the phase-space structure of our Galaxy. Stars coming from the same progenitor can be seen to

* E-mail: agenina@mpa-garching.mpg.de (AG)

“clump” in angular momentum – energy space (Helmi & de Zeeuw 2000; Gómez & Helmi 2010). Spatially, mergers can leave an imprint in the form of ‘shells’ and ‘streams’ which have been observed in the Milky Way and nearby galaxies (Quinn et al. 1996; Ibata et al. 2007b; McConnachie et al. 2009; Cooper et al. 2011; Bernard et al. 2016; Shipp et al. 2018; Martínez-Delgado et al. 2021). The identification of these features in the spatial distribution and kinematics of Milky Way’s stars, coupled with their chemical abundances, give clues to the accretion history of our Galaxy (Johnston et al. 2008; Bonaca et al. 2021). Recently, some of these properties have been used to determine that Milky Way underwent a merger with an object now known as *Gaia* Enceladus/*Sausage* (Helmi et al. 2018; Belokurov et al. 2018). Other progenitors of the present-day Milky Way have been inferred from the chemo-kinematics of the Milky Way’s accreted population of globular clusters (Kruijssen et al. 2019).

In recent years, the *Gaia* satellite (Gaia Collaboration et al. 2018, 2021) has uncovered a number of disrupted objects within the Milky Way through the coherent kinematics of their stripped stars. Tools such as STREAMFINDER (Malhan & Ibata 2018) have been used to discover such objects with proper motions and deep photometry. This approach has been effective at identifying a number of globular cluster streams within the Milky Way. Some of these have been associated with dwarf galaxies which now make up the stellar halo (Malhan et al. 2022). Nevertheless, finding evidence of disrupted dwarf galaxies in stellar motions has proven to be more difficult. This is because the large velocity dispersion in dark matter-dominated dwarf galaxies result in more kinematically hot streams, where the orbits of stripped stars can vary substantially from that of the dwarf (Helmi & White 1999). Moreover, due to their higher mass, dwarf galaxies tend to sink into the centre of the Galaxy by dynamical friction (Amorisco 2017). The stripped stars, particularly near the centre, become phase-mixed over time and the effectiveness of the integrals of motion in identifying coherent structures is then limited in the time-varying asymmetric potential of the Milky Way. For these reasons, it is the stars in the outer halo, with longer dynamical times, that likely hold clues on past mergers of our Galaxy.

The CDM paradigm, where the halo assembles largely through tidal stripping of smaller infalling objects, predicts that the majority of the stellar halo and at least a fraction of the dark matter halo have a common origin. It is thus possible that the properties of the Milky Way’s stellar halo can be used to investigate those of the dark matter. For instance, the extent of the stellar halo may be directly related to that of the dark matter. Moreover, phase-space features in the stars may also suggest equivalent features in the dark matter (Tissera & Scannapieco 2014; Herzog-Arbeitman et al. 2018). Local dark matter overdensities are important features for direct and indirect searches for the dark matter particle (Simpson et al. 2019; Necib et al. 2019; O’Hare et al. 2020).

In the spherical collapse model of the formation of virialized structures, overdensities in the early Universe gravitationally attract surrounding material, causing it to collapse and virialize, leading to the formation of ‘caustic’ shells of matter (Vogelsberger et al. 2009; Vogelsberger & White 2011), corresponding to the apocentres of successively accreted material, with their spacing dependent on the rate of growth of the dark matter halo (Gunn & Gott 1972; Fillmore & Goldreich 1984; Bertschinger 1985). Although this picture is simplified, structures modeled with N -body simulations match well analytical predictions (Zavala et al. 2008; Adhikari et al. 2014; Sugiura et al. 2020). In particular, the outermost shell, corresponding to the first apocentre of the most recently accreted material is related to the “splashback” radius of the halo and provides a physical

definition of the halo boundary (Diemer & Kravtsov 2014; Diemer et al. 2017). With the inclusion of hydrodynamical processes in cosmological simulations, it has become possible to follow the evolution of the stars and gas after accretion. Deason et al. (2020) have shown that together with the outermost ‘splashback’ radius, Milky Way analogues in the APOSTLE (Sawala et al. 2016; Fattahi et al. 2016), AURIGA (Grand et al. 2017) and ELVIS (Garrison-Kimmel et al. 2014) simulations also have a ‘second caustic’ in the dark matter, which roughly coincides with the visual extent of the stellar halo and is located at $\sim 0.6R_{200,m}$, or near $R_{200,crit}$. This second caustic is directly measurable as the steepest drop in the log-slope of the stellar density distribution or in its radial velocity profile. An observation of the “edge” feature could thus allow us to infer the size of the dark matter halo and its properties would be directly related to the accretion history of the Milky Way.

In this work, we investigate the origin of the ‘second caustic’ in the stellar and dark matter haloes of Milky Way / M31 analogues in APOSTLE simulations. In Section 2, we introduce the APOSTLE suite of simulations and provide some definitions that we will use throughout this work. We then split our sample of 10 galaxies into a ‘quiet’ subsample that is more Milky Way-like and an ‘active’ subsample that is more M31-like (Deason et al. 2013; Pillepich et al. 2014; Lancaster et al. 2019). In Section 3 we examine the historical build-up and present-day composition of the stellar and dark matter haloes of these analogue galaxies. In Section 4, we examine the phase-space properties of the ‘quiet’ and ‘active’ galaxies, focusing on the differences between the two and the relation to the phase-space properties of their dark matter haloes. In Section 5, we investigate the formation of phase-space features in the stellar and dark matter haloes, looking in particular at the mergers that contributed to their formation, their infall and tidal history. We comment on the halo and galaxy properties which influence the characteristics of the phase-space distribution. In Section 6, we discuss how observations of the luminous stellar component of haloes may be used to uncover the properties of the dark component and observational strategies that the present work suggests. In Section 7, we summarise our results.

2 SIMULATIONS

2.1 APOSTLE simulations

The APOSTLE (A Project Of Simulating The Local Environment) simulations are a suite of N -body hydrodynamical zoom simulations of environments resembling the Local Group (Fattahi et al. 2016; Sawala et al. 2016). Each simulation volume features a Milky Way - M31 analogue pair. The pairs of haloes were selected to match the observational constraints on the Local Group, such as the combined halo mass, galaxy separation, relative radial and tangential velocity and the velocities of nearby galaxies. The M_{200} values of the haloes range between 5×10^{11} and $2.5 \times 10^{12} M_{\odot}$. The high-resolution zoom region comprises a sphere of ~ 2.5 Mpc from the barycentre of the halo pair, within a 100^3 Mpc³ box. The suite consists of 12 volumes simulated at low and medium resolution, while 5 volumes have also been simulated at high resolution. In this work, we analyse these five simulations, giving us a sample of 10 Milky Way-mass galaxies. Their dark matter particle mass is in the range $2.5 - 5 \times 10^4 M_{\odot}$ and their gas particles have initial masses in the range $0.5 - 1 \times 10^4 M_{\odot}$; the gravitational softening length, $\epsilon_g = 134$ pc.

The APOSTLE suite was run with the P-GADGET-3 code (Springel 2005), assuming a WMAP-7 cosmology (Komatsu et al.

2011). A TREE-PM scheme is used to compute gravitational accelerations. Galaxy formation is modeled using the EAGLE code (Crain et al. 2015; Schaye et al. 2015). EAGLE solves hydrodynamic forces using the smoothed particle hydrodynamics (SPH) ANARCHY scheme (Dalla Vecchia & Schaye 2012; Schaller et al. 2015) and the pressure-entropy formalism (Hopkins 2013). The EAGLE model was calibrated to reproduce the $z = 0.1$ stellar mass function and galaxy sizes above $10^8 M_{\odot}$. The model includes cooling, star formation and evolution and feedback from supernovae, stellar mass loss, active galactic nuclei and radiation pressure (Wiersma et al. 2009a; Schaye 2004; Schaye & Dalla Vecchia 2008; Booth & Schaye 2009; Rosas-Guevara et al. 2015). A uniform ionizing background is turned on instantaneously at $z = 11.5$ (Haardt & Madau 2012). Cooling rates are computed for 11 tracked chemical elements (including hydrogen and iron), assuming ionization equilibrium in the presence of UV and X-ray backgrounds and the cosmic microwave background (Wiersma et al. 2009b).

Artificial fragmentation of the ISM is prevented by imposing a temperature floor through a polytropic equation of state. Star formation has a metallicity-dependent density threshold that effectively ranges between $n_H = 0.1 - 1 \text{ cm}^{-3}$. Star formation is also pressure-dependent and follows the Kennicutt-Schmidt star formation law (Schmidt 1959; Kennicutt 1998). A stellar particle within the simulations represents a simple stellar population following a Chabrier (2003) initial mass function. Feedback from star formation is implemented using the stochastic thermal prescription of Dalla Vecchia & Schaye (2012).

EAGLE has been shown to reproduce the evolution of the stellar mass function, colours and magnitudes of galaxies, scaling laws of galaxy populations. The EAGLE-REF model, used in APOSTLE, produces Milky Way and M31 analogues of lower stellar mass than suggested by observations, as discussed in Fattahi et al. (2016). At the same time, APOSTLE provides a good match to the abundances of satellites and dwarf galaxy scaling relations within the Local Group (Sawala et al. 2016; Fattahi et al. 2016; Campbell et al. 2017), including dwarf metallicities (Genina et al. 2019).

2.2 Classification of stellar and dark halo components

In this work we investigate the build-up of the accreted stellar and dark matter haloes of Milky Way-mass galaxies. In order to do so, we must define a redshift-dependent halo boundary. A possible definition of this is the splashback radius; however, the exact definition of this radius is uncertain and complicated by the fact that we are studying group environments. Instead, we opt to use the radius enclosing 200 times the mean matter density of the Universe at each redshift, $R_{200,m}(z)$, as our definition of the halo boundary. This is also motivated by the finding that the splashback radius tends to be close to this value, and much further out than $R_{200,\text{crit}}$ (Diemer & Kravtsov 2014). We identify substructures in our simulations using the HBT+ algorithm (Han et al. 2018). For each stellar particle within $R_{200,m}(z)$ of either of the main haloes at $z = 0$, excluding those that are identified as bound to satellite haloes, we track the particle back in time until it is identified as being bound to a halo or a subhalo that is not one of the two main haloes. We classify all stellar particles which are bound to the Milky Way / M31 analogue at the time of their birth as ‘disk’ particles. A negligible fraction of stellar particles are never identified as bound in the available snapshot outputs and we exclude these particles from the analysis.

For the dark matter halo particles, we also track each particle back in time until there is a substructure match. However, unlike the stellar particles, a large fraction of dark matter comes from

smooth accretion. This includes unresolved haloes and individual dark matter particles that were never bound to a subhalo. All dark matter particles which are part of one of the main haloes at $z = 0$ and for which there is no historical substructure match are classified as the ‘smooth’ dark halo component.

We also must decide how to treat mergers of substructures which occur *inside* of the Milky Way/M31 halo. We opt to count the subhaloes that merged while within the halo as a single object, even if particles had been stripped within the Milky Way/M31 analogue prior to the merger. Additionally, we impose a merging criterion. Namely, we consider a subhalo to have merged with another subhalo when it has lost all of its bound mass, retaining only an ‘orphan’ particle. To be merged with a subhalo, this particle must lie within the maximum subhalo radius, defined by the location of subhalo’s furthest bound particle. We further ensure that this particle is gravitationally bound to the subhalo. We establish whether the orphan particle is bound by comparing its relative velocity with respect to the centre of the subhalo to the subhalo’s local escape velocity. The latter is computed by performing an NFW profile fit to the subhalo out to the maximum subhalo radius. Finally, at $z = 0$, we ‘climb the tree’ and ensure all orphans representing substructures and substructures-of-substructures are assigned to the main progenitor.

Finally, due to the time spacing of outputs of our simulations some stellar particles may be incorrectly identified as formed *in-situ* within the Milky Way/M31 analogues if the star-forming gas of an accreted satellite has been stripped between two simulation snapshots (Zolotov et al. 2009). To correct for this, we take all stars that are identified as *in-situ* at birth and check if their parent gas particle was bound to the Milky Way/M31 analogue or a satellite galaxy in the previous snapshot and assign its origin accordingly.

3 THE BUILD-UP OF THE ACCRETED STELLAR AND DARK MATTER HALOES

3.1 Halo composition

We begin by studying the build-up of the accreted stellar and dark matter haloes of Milky Way-mass galaxies. Dark-matter-only (DMO) simulations show that major mergers (mass ratio $> 1 : 10$) contribute only 20 per cent of the dark matter halo mass in Milky Way-mass galaxies, with the majority made up of the ‘diffuse’ component, which includes unresolved haloes and minor mergers in roughly equal amounts (Wang et al. 2011). However, this picture need not be reflected in the stellar halo because only the most massive haloes will form a galaxy which can subsequently be deposited into the stellar halo of the Milky Way. The power-law form of the CDM mass function implies that small dwarfs are more abundant than large ones; however it is the less numerous, more massive, haloes that contain the most stellar mass. This opens up the question of whether most of the stellar halo is made up of stars gained in mergers with many small dwarfs or few large ones and whether these are surviving or disrupted at the present day. These questions have in the past been tackled with semi-analytical approaches (Cooper et al. 2010; Deason et al. 2016; De Lucia & Helmi 2008), as well as hydrodynamics simulations (Monachesi et al. 2019; Fattahi et al. 2020; Santistevan et al. 2020). These have generally favoured Milky Way stellar haloes that are dominated by stars from a few, massive dwarfs that are already disrupted. In the following, we investigate whether these findings hold in the APOSTLE simulations. We emphasize that in this work we only consider the the stellar halo stars

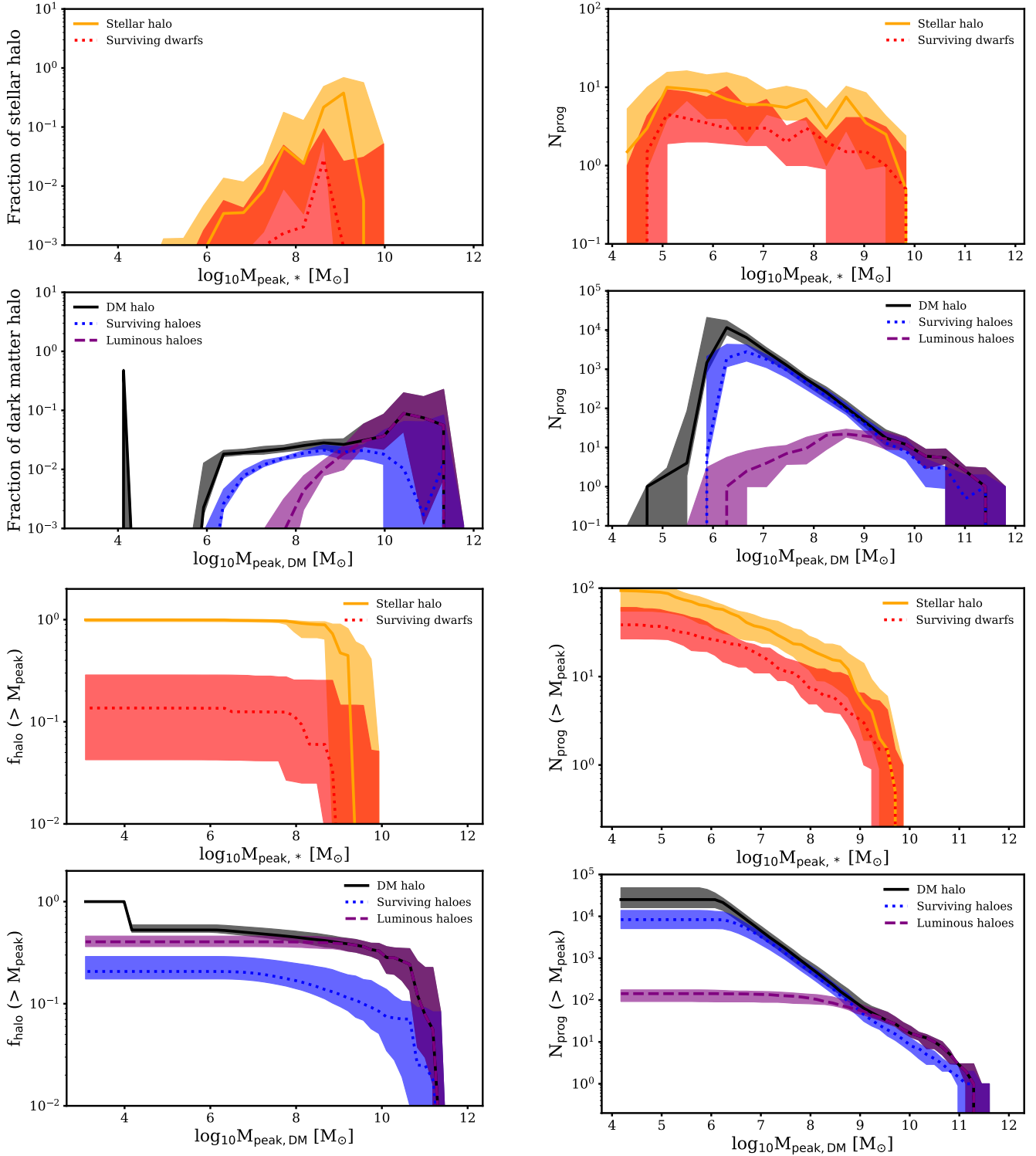


Figure 1. Composition of the stellar and dark matter haloes of Milky Way-M31 analogues, defined by the stars and dark matter that are not bound to any subhalo within $R_{200,m}$. *Top left:* the fraction of stellar and dark matter haloes made up from progenitors of a given peak stellar and dark matter masses. Thick lines show the median and the bands span the minimum and maximum values of the entire sample. Yellow corresponds to the make-up of the entire stellar halo and red identifies the objects that survive to the present day. Black shows the entire dark matter halo, purple the subhaloes that have hosted stars in the past and blue the subhaloes that survive to the present day. The peak near $\sim 10^4 M_{\odot}$ corresponds to the typical mass of a dark matter particle in APOSTLE and shows the contribution of the smooth component. *Top right:* halo composition in terms of the number of contributing objects of each peak stellar/halo mass. *Bottom left:* the fraction of the halo made up of objects above a given peak mass. *Bottom right:* number of dwarfs/subhaloes above a given peak mass contributing stars and dark matter to the halo.

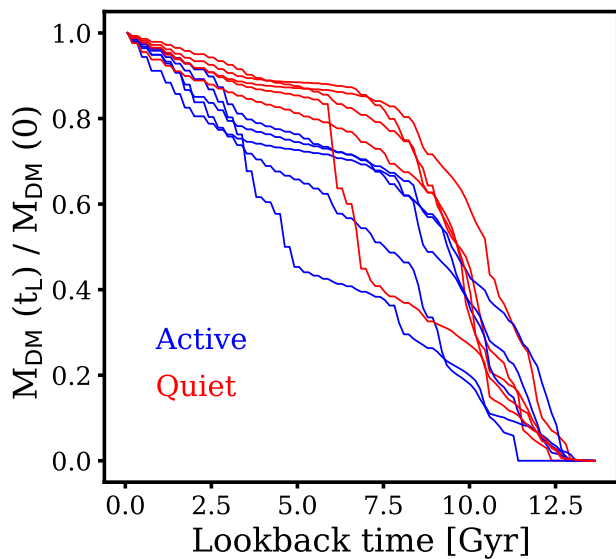


Figure 2. The dark matter assembly histories of the Milky Way/M31 analogues in our simulations. The haloes are split into “active” and “quiet” based on their recent accretion history (within the last 6 Gyr), namely “quiet” haloes that were assembled early and “active” haloes that show fast recent growth.

contributed by the accreted dwarf galaxies and ignore the *in-situ* component contributed by the stars scattered from the Milky Way disc (Belokurov et al. 2020). A number of previous works have found that this component becomes subdominant beyond ~ 50 kpc (Zolotov et al. 2009; Font et al. 2011, 2020; Santistevan et al. 2020), we therefore exclude it from our analysis, which instead focuses on understanding the origin of the phase-space features defining the “edge” of the stellar halo.

3.1.1 Stellar halo composition

In Fig. 1 we show the make-up of the stellar and dark matter haloes in terms of the peak (that is the maximum value attained) stellar and dark matter masses of infalling dwarfs (upper left) and in terms of the number of dwarfs at a given peak mass (upper right). The peak in the fraction of the stellar halo contributed by objects of a given mass occurs at peak stellar mass of $M_{\text{peak},*} \sim 10^9 M_{\odot}$, where, on average, dwarfs with this stellar mass make up ~ 40 per cent of the stellar halo. However, it can also be seen that the scatter is rather large and some of the Milky Way analogues either accreted no objects of this stellar mass, or only accreted them at late times, when the amount of stellar stripping was insufficient to contribute any significant mass to the halo (surviving dwarfs are shown by the dotted red line). On the bottom left of Fig. 1, we show the cumulative version of this figure. Evidently, dwarfs with peak stellar mass of above $10^8 M_{\odot}$ contribute at least 70 per cent of the stellar halo. We also note that typically less than 20 per cent comes from dwarfs surviving at $z = 0$. The stellar mass function of the dwarf progenitors (bottom right of Fig. 1) suggests there are approximately 20 progenitors with stellar mass above $10^8 M_{\odot}$ (7 surviving) and 6 above $10^9 M_{\odot}$ (3 surviving) in a typical Milky Way analogue. These results are consistent with the work of Elias et al. (2018) that used Illustris simulations, but there are also differences in two aspects. One is that they find no contributing satellites above $\sim 10^{9.5} M_{\odot}$ in stellar mass, while we have 1-2 contributors. We attribute this difference

to their sample selection of Milky Way-mass galaxies that lack a massive LMC-like satellites at the present day. Another difference is that below $\sim 10^7 M_{\odot}$ their contributing number of satellites is higher than ours. We believe that this is due to our choice of not counting dwarf galaxies that merge with a bigger galaxy within the Milky Way. Elias et al. (2018) also have generally lower counts of surviving satellites at all masses than presented in this work, which we believe is a consequence of mass resolution in their simulations, which is a factor of 10^2 lower and likely results in enhanced satellite disruption (van den Bosch & Ogiya 2018). Conversely, the work of Fattahi et al. (2020) using AURIGA simulations returns mass functions that have a similar shape to ours, but have a systematically lower normalization for both surviving dwarfs and all progenitors, while still agreeing with our results within the scatter of Milky Way analogue mass functions. Their method of counting dwarfs contributing to the halo is very similar to ours, so the discrepancy likely arises from the fact that these authors only count the dwarfs accreted after $z = 3$ ¹ and that the discs in AURIGA are more effective in disrupting the satellite population than APOSTLE (Richings et al. 2020), though the differences are important for substructures with $M_{\text{DM}} < 10^8 M_{\odot}$ which should in principle remain dark. In any case, we have verified that restricting our count of halo contributors to those infalling after $z = 3$ places our results in agreement with Fattahi et al. (2020).

3.1.2 Dark matter halo composition

We now focus on the dark matter. Immediately, we see that the tallest peak in dark matter halo contribution is at $\sim 10^4 M_{\odot}$, which is the dark matter particle resolution in our simulations. This is the contribution of the ‘smooth’ and ‘unresolved’ component. Among the resolved bound substructures, it can be seen that significant fractions of the dark matter halo mass come from dwarfs with peak halo mass $\sim 3 \times 10^{10} M_{\odot}$. The purple histogram highlights subhaloes that have hosted stars in the past. It is evident that all objects above $\sim 10^{10} M_{\odot}$ hosted stars in the past. The cumulative version of this plot (bottom left of Fig. 1) confirms the previous findings that nearly half of the dark matter halo is in a ‘smooth’ component and the other half in bound structures. It can also be seen that about 40 per cent of the dark matter halo mass has come from objects that have hosted stars in the past and of those, nearly all had halo mass above $10^9 M_{\odot}$, consistent with the hydrogen cooling limit arguments, while 30 per cent of the halo mass comes in subhaloes of peak mass greater than $10^{10} M_{\odot}$. The dark matter haloes of Milky Way-mass galaxies had 100-200 luminous contributors (with stellar masses $\gtrsim 10^3 M_{\odot}$), though only 10-20 of them make up the majority of the stellar halo.

3.2 Active and quiet dark matter halo assembly

Before we proceed to examine the radial distributions of various components of the stellar and dark matter haloes, we split our sample of Milky Way and M31 analogues into those with ‘active’ formation histories (haloes which are still rapidly increasing in mass down to $z = 0$) and those with ‘quiet’ formation histories (those whose halo growth rate over the past few gigayears is slow). We

¹ This choice stems from unreliability of determining the main progenitor at early times. In this work, we rely on the definition of the main progenitor by the HBT+ halo finder, which is based on the mass and specific kinetic energy of progenitor candidates.

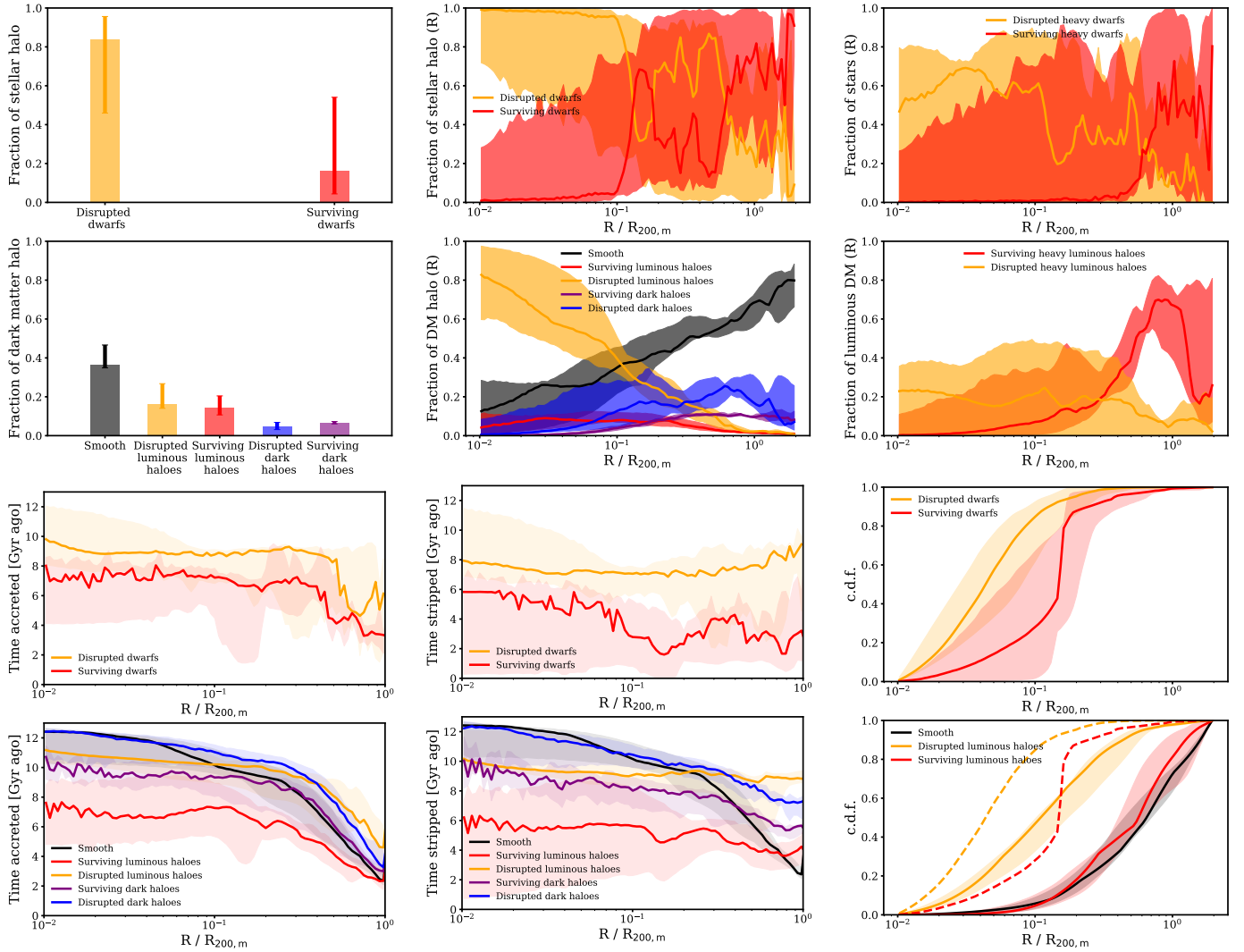


Figure 3. Radial distribution of the stellar and dark matter haloes of *active* galaxies. The upper panels of each subplot show the stars and the bottom panels the dark matter. Yellow identifies luminous haloes that are fully disrupted by $z = 0$, red shows luminous haloes that survive, blue shows disrupted dark haloes that never hosted stars, purple shows surviving dark haloes that never hosted stars and black shows dark matter that was never bound to a subhalo (i.e. the “smooth” component). *Top left:* bar chart showing the fraction of the halo made up by each component. The height corresponds to the median across the sample of active galaxies and the error bars bracket the minimum and maximum values in the sample. *Top centre:* The fraction of the halo at each radius contributed by each of the components. Solid lines show the median of the sample and the band shows ranges for the entire sample. *Top right:* The fraction of the halo at each radius made up by disrupted (yellow) and surviving (red) *massive* luminous haloes, defined as the dwarfs that make up 50 per cent of the stellar halo ($\sim M_{\text{peak},*} > 10^9 M_{\odot}$). *Bottom left:* The lookback time at which various halo components as a function of radius first entered $R_{200,m}(z)$. *Bottom centre:* The lookback time at which various halo components as a function of radius were stripped from their haloes. For the smooth component we display the accretion time as in the panel on the left. *Bottom right:* the cumulative distribution function of the stars and the dark matter stripped from fully disrupted and surviving dwarfs. In the bottom panel, the dashed lines show the median of the stars.

make this sample separation for two reasons. One is that we expect that the radial distributions of debris from surviving and disrupted dwarfs will be different in these two cases – the locations of stars coming from surviving dwarfs are expected to peak away from the centre of the galaxy and the disk. Secondly, the sample separation is motivated by the distinction in the inferred formation histories of the Milky Way and M31. The Milky Way is believed to have been relatively quiet (Deason et al. 2013; Pillepich et al. 2014; Lancaster et al. 2019), while M31 is still actively assembling. In Fig. 2 we show the dark matter halo assembly histories of our Milky Way/M31 analogues; the subsamples are shown in blue (active) and

red (quiet). The quiet sample is characterised by analogues that had formed ~ 80 per cent of their mass 6 Gyr ago and had a slow growth rate after that. In contrast, the ‘active’ haloes formed ~ 80 per cent of their mass approximately 3 Gyr ago and their growth thereafter is fast. We find that lower-mass haloes in our sample tend to be ‘active’, while higher-mass haloes are typically ‘quiet’. This may seem surprising from the hierarchical structure formation considerations. This occurs because our “zoom” simulations are constrained to have haloes in the Milky Way / M31 mass range. If we instead define recent accretion history as that within the last 8.5 Gyr (Diemer & Kravtsov 2014), we recover the expected trend where high-mass

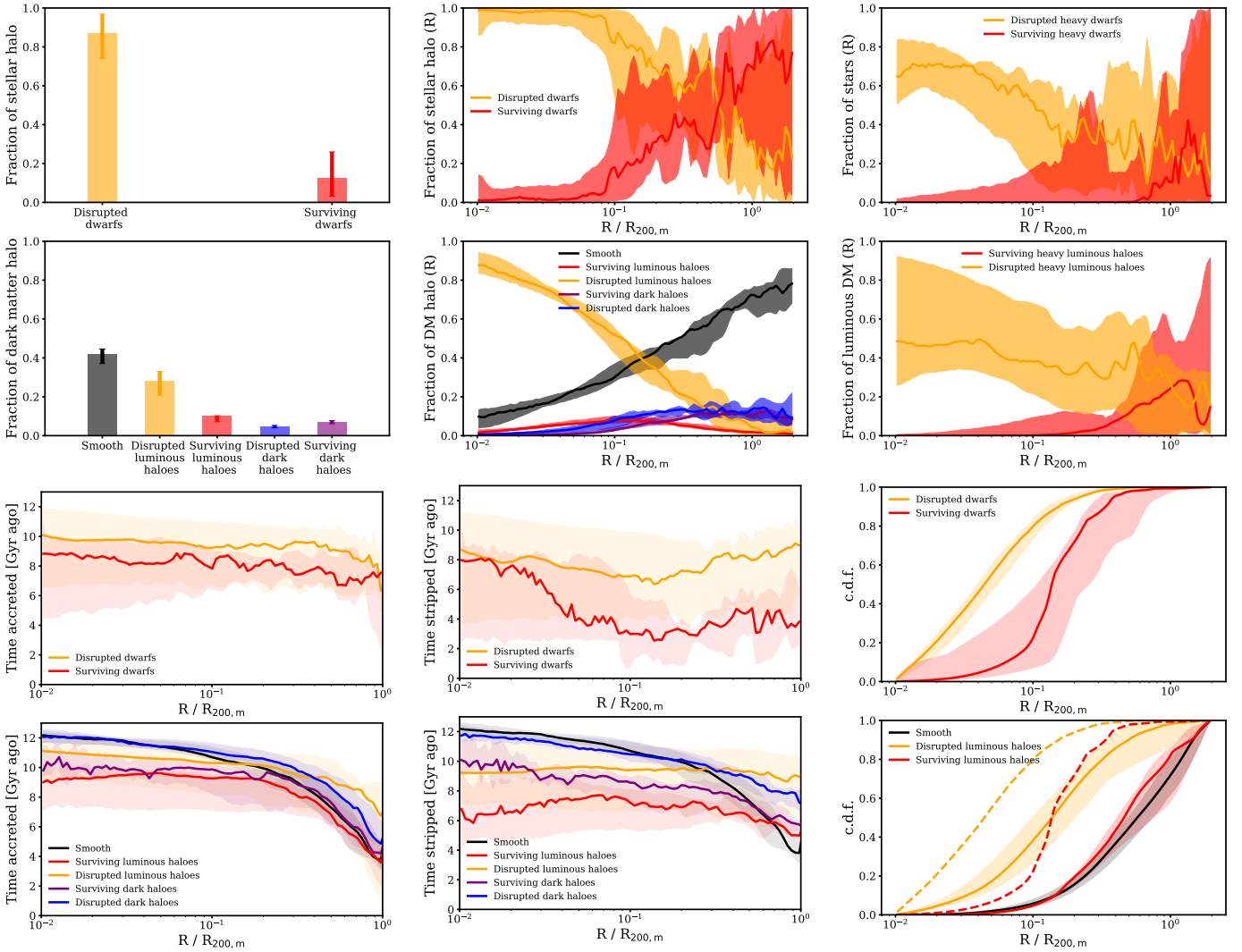


Figure 4. Same as Fig. 3, but for *quiet* Milky Way/M31 analogues.

haloes have more active assembly histories. We find no correlation between the assembly histories of the two main haloes in each simulation volume.

There are two extreme examples in both of these categories. Within the ‘active’ sample there is a galaxy that has built up nearly 50 per cent of its halo mass in the last 5 Gyr. This is due to a very recent major merger. This galaxy is an outlier in this category, but is, of course, formally ‘active’. Within the ‘quiet’ sample we see a galaxy which had two large mergers ~ 7 Gyr ago and has since assembled only about 10 per cent of its final mass. This is distinct from the rest of the ‘quiet’ sample, where nearly all of the final halo mass has been built up ~ 9 Gyr ago. In the following, we keep these galaxies in their respective categories, bearing in mind that the rest of galaxies in each sample have very similar assembly histories, so that our outliers will likely not affect the median radial distributions, but would instead contribute to the scatter.

3.3 Radial distribution of halo components

We have so far shown that the stellar halo of Milky Way-like galaxies is dominated by stars stripped from a few massive dwarfs that are primarily disrupted by $z = 0$, while the dark matter halo is dominated by a smooth, unresolved component. We summarize these findings in the top left of Figs. 3 and 4 for the active and quiet Milky Way / M31 analogues, respectively. It is clear that the smooth component is the dominant contribution to the dark halo. In both active and quiet samples the disrupted dwarfs dominate the stellar halo, but surviving dwarfs contribute more significantly in the active sample. Interestingly, while the mean contributions to the stellar halo of the disrupted and surviving dwarfs are similar in the quiet and active samples, there are clear differences in the contributions of these objects to the dark matter. Specifically, disrupted and surviving dwarfs contribute roughly the same amount of dark matter in the ‘active’ sample, yet they contribute very different fractions to the stellar halo. This suggests that substantial amounts of dark matter have been stripped from surviving dwarfs, but their stellar component has not been significantly affected. We now investigate how these components are distributed within the haloes. We aim to establish,

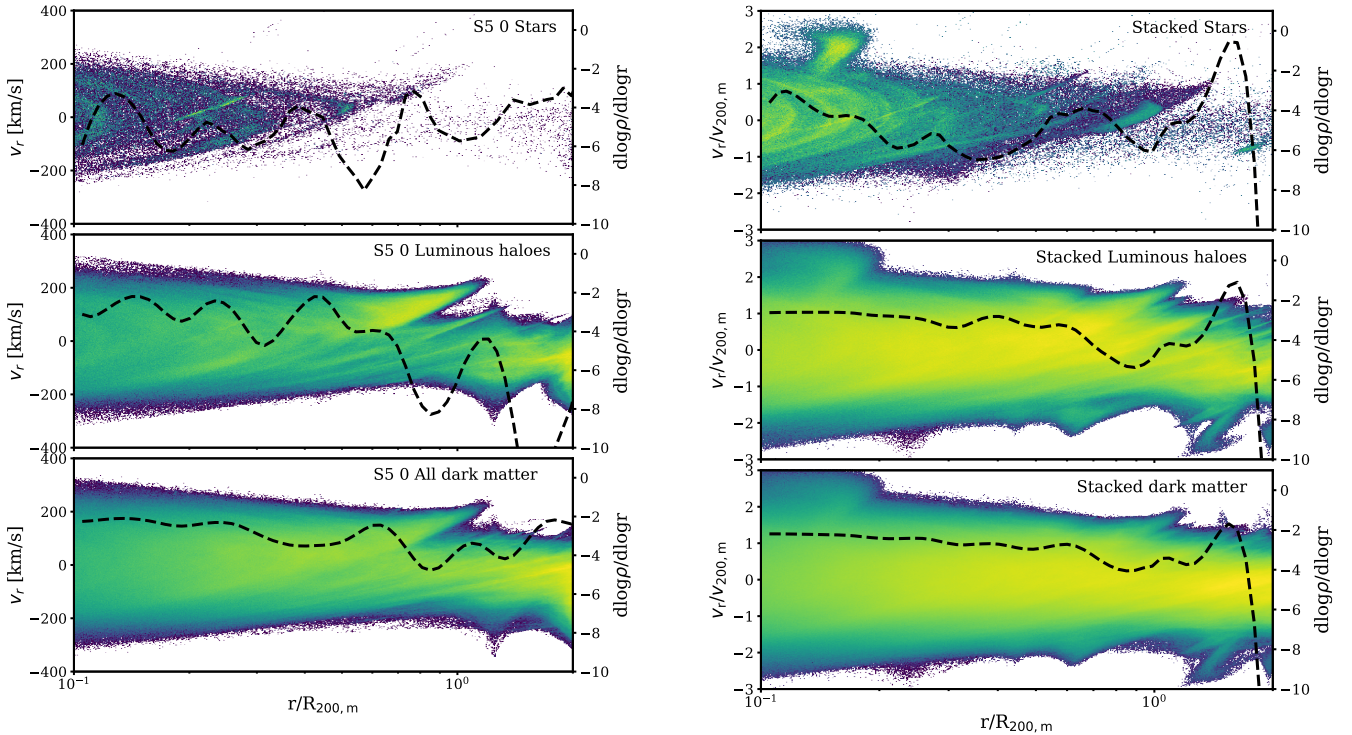


Figure 5. The radial velocity - distance (or “phase-space”) diagrams of *active* Milky Way/M31 analogues. *Left panel:* individual example of an active galaxy, where in the top we display the entire stellar component, in the middle the dark matter stripped from objects which have in the past hosted stars and in the bottom all of the dark matter in the halo, excluding bound subhaloes. The dashed lines in each case show the log-slope of the density profile. *Right panel:* the sample of active galaxies stacked together. The dashed lines show the log-slope of the density profile of the stack. The radial velocity axis is normalized by the circular velocity at $R_{200,m}$.

for instance, whether the smooth halo component is dominant at all radii or only in the outskirts of haloes and whether these radial distributions are different in active and quiet Milky Way / M31 analogues.

In the top-centre panels of Figs. 3 and 4, we show the fraction of the stellar and dark matter haloes that each component contributes at a given radius. In both active and quiet samples, disrupted dwarfs make up almost all of the stellar halo up to $0.1R_{200,m}$ and remain dominant out to $\sim 0.8R_{200,m}$ with scatter, while surviving dwarfs contribute most of the material outside that radius. This is an agreement with fig.6 of Fattahi et al. (2020), who find that massive, destroyed dwarfs dominate the contribution out to $\sim 100\text{-}200$ kpc in AURIGA Milky Way analogues ($\sim 0.3 - 0.5R_{200,m}$ in our simulations).

In the active sample, there is a small radial range between 0.1 and $0.2 R_{200,m}$ where material stripped from surviving dwarfs dominates on average, providing ~ 65 per cent of the visible matter in the halo. This is material stripped recently (within the last 2 Gyr) from surviving dwarfs that wandered close to the centre of the halo. Interestingly, we do not see a corresponding peak in the dark matter contributed by surviving luminous haloes. The reason for this is the outside-in stripping of infalling dwarfs (illustrated in the bottom panels of Figs. 3 and 4), that makes the stripping times of the dark matter and the stars different.

For the dark matter, in both active and quiet samples, we see that the smooth component makes up only a small fraction of the inner dark matter halo (~ 10 per cent at $0.01R_{200,m}$, roughly the Milky Way half-light radius); the majority of the dark matter has

come from the dark matter of disrupted dwarf galaxies. The smooth component becomes dominant at $\sim 0.2R_{200,m}$, but the dark matter from disrupted dwarf galaxies is still a major contributing component out to $\sim 0.3R_{200,m}$ in the active sample and $\sim 0.6R_{200,m}$ in the quiet sample.

3.4 Radial contribution by mass

We have now established that it is the most massive, luminous dwarfs that make up the majority of the stellar halo. However, it is still unclear whether this is true over the entire radial extent of the halo. It could be the case that the massive dwarfs dominate only in the centre, where most of the stars are expected to be deposited in a merger, while the more numerous small dwarfs with longer dynamical friction sinking timescales deposit their stars in the outer halo, dominating the local stellar content. To address this question, we split the disrupted and surviving dwarfs by mass, such that massive dwarfs above a given threshold mass make up 50 per cent of the stellar halo. We then show the radial contribution of each component to the stellar halo.

In agreement with the upper left panel of Fig 1, we find that this threshold peak stellar mass is typically $\sim 10^9 M_\odot$ and ranges between $10^8 - 10^{9.5} M_\odot$ for our Milky Way / M31 analogues, corresponding to LMC/SMC-mass dwarf galaxies. It can be seen that massive dwarfs, surviving and disrupted, contribute over ~ 30 per cent of the mass at all radii. The massive disrupted dwarfs clearly dominate the stellar halo content within $0.1R_{200,m}$. The contribution of the most massive dwarfs diminishes between 0.1

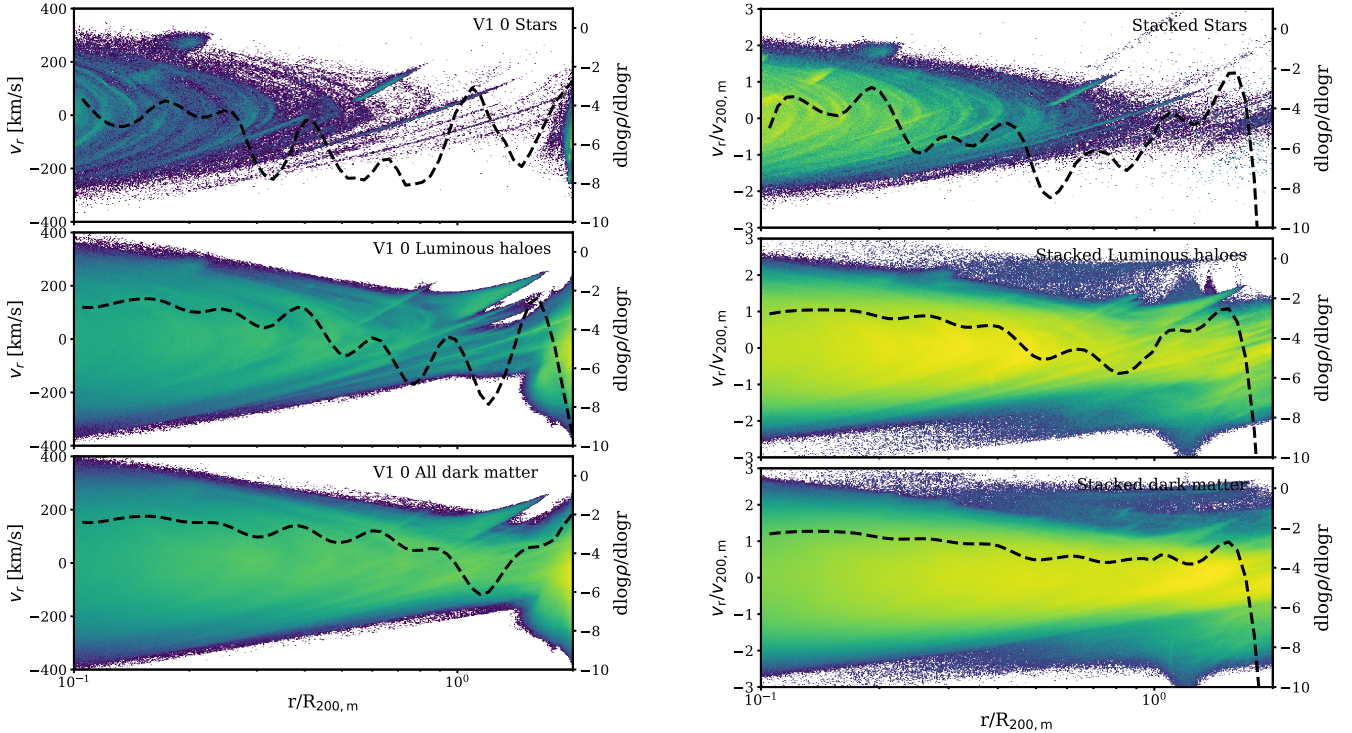


Figure 6. Same as Fig. 5, but for the *quiet* sample of Milky Way/M31 analogues.

and $1R_{200,m}$. Indeed, the smaller dwarfs become more important in the ‘intermediate’ halo regions. This is likely because their orbits are relatively more tangential due to the reduced effects of dynamical friction. We do find that the debris stripped from lower-mass dwarfs has *on average* larger orbital apocentres, however the most massive haloes typically have larger *maximum* apocentres due to their larger size and velocity dispersion. It is also clear that the peak in the contribution of surviving dwarfs seen between 0.1 and $0.2R_{200,m}$ in active galaxies (top-centre panel) is not caused by the most massive dwarfs that entered the halo. This is not surprising, given that in Fig. 1 we saw that the peak masses of disrupted dwarfs are on average greater than those of surviving ones. In other words, it is likely that the most massive contributor to the Milky Way’s stellar halo (in terms of peak stellar mass) has already been disrupted.

This picture is somewhat different in the dark matter, where the most massive mergers contribute typically no more than 30–40 per cent of the dark matter coming from luminous subhaloes. This is most likely a consequence of the stellar mass–halo mass relation (Behroozi et al. 2013; Moster et al. 2013), whereby dark matter dominates the mass of smaller dwarfs (e.g. dwarf spheroidals and the ultra-faints) more so than in the dwarf irregulars (e.g. LMC). As a result, smaller dwarf galaxies contribute a larger fraction of their mass in dark matter than the larger dwarfs. Overall, it is remarkable that out to the outermost radius within the halo, the material of 3–4 massive dwarfs can make up nearly half of the stellar halo.

3.5 Radial gradients in accretion and stripping time

We now examine the radial accretion time gradients in the stellar and dark matter haloes, both regarding the time of entry into $R_{200,m}$ and

the time when the material was stripped from infalling subhaloes² (lower panels in Figs 3 and 4).

The radial distribution of the stellar accretion times shows a remarkably flat profile both for disrupted and surviving dwarfs out to large radii, in both subsamples. This either suggests that the majority of dwarfs contributing to the stellar halo were accreted at roughly the same time or that the stellar halo is dominated by one or two objects. In the quiet sample, this may be the case, as few disrupted dwarfs make up nearly half of the stellar halo at all radii.

For the active sample, above $\sim 0.4–0.5R_{200,m}$ the stellar halo has an increasing contribution from more recently accreted objects, both surviving and disrupted. This is in agreement with the findings of Font et al. (2011), using GIMIC simulations, who find a declining profile in accretion time as a function of radius for their Milky Way analogue. When looking at the radial stripping time (bottom centre of Fig. 3), we begin to see a mild gradient, whereby material near the halo centre was stripped earlier and the material in the outskirts later on, before the slope flattens, such that above $0.2R_{200,m}$ the halo material was stripped at approximately the same time. This suggests either that the material deposited in the outer parts of the halo from a given dominant object was stripped later on (which seems unlikely as we expect the infalling dwarfs to spiral towards the centre and deposit their stars there), or that the outer regions of the halo are dominated by dwarf galaxies that came on wider orbits, allowing their stars to be stripped later and at larger radii.

Overall, for the disrupted dwarfs we observe an offset between the accretion and stripping times of approximately 2 Gyr, while for surviving dwarfs this difference amounts to ~ 5 Gyr, suggesting

² The stripping time is not defined for the smooth halo component, so instead we use the time when these particles entered $R_{200,m}(z)$.

that the surviving dwarfs are harder to strip due to the particulars of their mass, the mass of the Milky Way analogue and the orbit.

For the dark matter, we see that the ‘smooth’ component in the inner regions is likely of primordial origin, while in the outer regions, where it dominates, the smooth component was deposited into the halo more recently. The latter is, however, also true for other constituents of the dark matter halo, where the outer regions are made up of dark matter accreted recently. Interestingly, the radial distributions suggest that in the outermost regions the dark matter particles had been stripped prior to entering $R_{200,m}$. We also see this odd behaviour for the stars that came from dwarfs that are disrupted.

This may be in line with the findings of Wang et al. (2011), who suggest that some of the “smooth” dark matter component in the halo could have come from previously bound structures that lost dark matter particles during a merger prior to infall. Moreover, considering that we are analysing Local Group-like environments, it is plausible that some of the material could have come from subhaloes that had been previously stripped within the companion halo, then ejected, before infalling into the Milky Way analogue. However, we have found that these objects make up no more than 10 per cent of the material currently outside $R_{200,m}$.

Instead, there are two main sources for the apparent inconsistency between the ‘stripping’ and the ‘accretion’ time. The first contributes at small and large radii and is due to dwarfs that merge with the Milky Way analogue at early times, when $R_{200,m}(z)$ is rather small and thus it takes a while for some of the dark matter particles, which become unbound during the merger, to formally cross $R_{200,m}(z)$ and therefore to be identified as having been “accreted”. This is particularly likely when the incoming dwarf itself is in the process of assembly and has an extended halo of loosely bound material. The second source is more important in the outermost regions of the halo and consists of massive, LMC-like, dwarfs that have entered the halo recently, so that some of the particles still have not crossed $R_{200,m}(z)$. In both cases, the wide spread in particle binding energies in these massive dwarfs can lead to a sufficiently small tidal radius, and the dark matter can become unbound prior to crossing $R_{200,m}(z)$.

It is additionally interesting to note that the discrepancy between the accretion and stripping times is more pronounced in active galaxies than in the quiet sample. This may explain why the disrupted dark haloes contribute more in the active galaxies near $R_{200,m}$ than they do in the quiet sample. As the active sample grows significantly in dark matter in the last 3 Gyr, it is likely that these dark haloes were ‘pre-processed’ by large objects that entered $R_{200,m}$ at late times.

It is clear that the central component is made up of stars stripped earlier, while the outer halo is made up of stars stripped later, which is also the case for the dark matter. However, one can also see that all radii, for disrupted and surviving dwarfs, the dark matter is stripped earlier than the stars. In the bottom right of Figs. 2 and 3, we compare the cumulative distributions of stars and dark matter stripped from disrupted and surviving dwarf galaxies. It can be seen that the stars are significantly more centrally concentrated than the dark matter, with a half-mass radius of $\sim 0.05R_{200,m}$ for the disrupted dwarfs, compared to $\sim 0.1R_{200,m}$ for the dark matter. Similarly, half of the mass in stars stripped from surviving objects is at $\sim 0.15R_{200,m}$ for the stars and $\sim 0.5R_{200,m}$ for the dark matter. This reinforces the idea that dark matter in dwarf galaxies typically gets stripped earlier and more efficiently than the stars.

4 PHASE-SPACE FEATURES IN THE STELLAR AND DARK MATTER HALOES

4.1 The radial velocity – distance diagram

In this Section we examine some of the orbital properties of the stars and the dark matter in the halo. On the left of Fig. 5 we focus on one example of an active halo. In the top panel, we show the $v_r - D$ diagram for all the stars in the halo (i.e. stars stripped from dwarf galaxies). In the centre we show dark matter that has come from luminous haloes and at the bottom we show all dark matter, including the smooth component. Similarly, in the left panel of Fig. 6, we show an example of a quiet galaxy. The dashed black lines show the computed log-slope of the density profile. These log-slope profiles are of interest in establishing the “splashback” radius of the dark matter and the “edge” of the galaxy, corresponding to minima in the log-slope of the profiles.

In order to compute the log-slope profiles, we follow the procedure of Deason et al. (2020). Namely, we bin the particles in 75 radial \log_{10} -spaced bins and in 11 angular-spaced bins. Since we consider Local Group-like systems, the splashback radii of the two main haloes may overlap. In order to circumvent this, we discard the angles $\cos(\theta) < -0.6$ and $\cos(\theta) > 0.6$ measured from a vector joining the two halo centres. For each radial bin, we then take the median of all bins in angle. Furthermore, we apply the fourth-order Savitzky-Golay filter (Savitzky & Golay 1964) over the 15 nearest bins to smooth the density profiles and compute the log slope. We use the same number of bins for the stars and for the dark matter. Note that we use a greater number of radial and angular bins than Deason et al. (2020), who analysed a lower-resolution version of APOSTLE³.

Examining the two examples visually, it is clear that ‘quiet’ galaxies are more structured in phase space, with clear ‘shells’ of particles moving on similar orbits. The ‘active’ galaxy exhibits less clear structure, with only some shells visible. In the outer regions, the particles stripped from currently surviving objects are also visible. These correspond to ‘streams’ one would observe stemming from dwarfs like Sagittarius. We note that these are less likely to contribute to the fluctuations in the log-slope profile, as in computing these profiles we take the angular average for a given bin in distance.

In the log-slope profile of the stars, several features are visible, with log-slope values < -6 . The dark matter, on the other hand, is smoother than the stars on this diagram. Some shells can be seen, but these are hard to distinguish from the background. In the log-slope profile, one can clearly see the splashback radius just outside $R_{200,m}$ in the quiet example, and slightly inside $R_{200,m}$ in the active example (where the log-slope drops to -4); this is consistent with the results of Diemer & Kravtsov (2014). Numerous other minima in the log-slope of the dark matter can also be seen, which seem to coincide roughly with the features in the stars, interestingly including the splashback feature.

The similarities in the orbital properties of the dark matter and the stars can be seen more clearly if we only select the dark matter coming from stripped luminous haloes (which, we note, is

³ Since we take a median of the angles, the ‘edge’ of the galaxy we infer is defined by particles that are generally well phase-mixed by the present day, rather than by potentially denser but highly anisotropic particle distributions arising from very recent accretion events (Mansfield et al. 2017). We have also carried out convergence studies, varying the number of radial and angular bins and found that the locations of the steepest log-slope minima do not vary significantly so as to affect the conclusions of this work.

comparable in amount to the smooth component, though the latter is dominant in the outer regions). This is shown in the middle left panels of Figs. 5 and 6, where it is clear that ‘shells’ of dark matter closely follow those of the stars and the features in the log-slope of the density profile are significantly more pronounced.

As in Deason et al. (2020), we see a pronounced feature in the log-slope of the stars at $\sim 0.6R_{200,m}$, for both active and quiet examples. In fact, several features are seen of comparable log-slope. We note that since Deason et al. (2020) analyzed the lower-resolution version of the APOSTLE simulations, some of the drops in the log-slope would likely combine into a single feature in their analysis. Likewise, if we reduce the number of radial bins, nearby log-slope features can merge into one, while varying the number of angular bins can result in different steepness of the log-slope caustics.

We now explore whether any of the log-slope features are common among our samples of active and quiet Milky Way analogues. For this, we stack the haloes in each subsample, weighting each particle by the inverse of the total stellar/dark matter halo mass within $R_{200,m}$ of the halo. We additionally normalize the radial velocity by the value of the circular velocity at $R_{200,m}$, to give equal weight to each Milky Way analogue. We then compute the log slope. We find the steepest feature in the log-slope of the stars between $0.5-0.6R_{200,m}$ for the quiet sample, and at $0.4R_{200,m}$ for the active sample. Note that this reflects the radii at which the contributions of disrupted luminous haloes are important in the two samples.

In Fig. 7 we demonstrate the similarity between the local minima in the log-slope profile of the stars and the dark matter. For each minimum in the stars, we find the nearest minimum in the dark matter (blue squares). We see that the minima in the log-slope of the stars often have a nearby minima in the log-slope of the dark matter. Equivalently, the (over/under)densities in the stellar distribution can be associated with (over/under)densities in the dark matter. We do, however, see some differences at small radii. This is a by-product of the noise in the distribution of the halo stars, compared to a much smoother distribution of the dark matter in the inner regions, given the binning we use to compute the profiles.

Red star symbols show the location of the steepest drop in the log-slope of the stars. The black squares show the splashback radius identified in the log-slope profile of the dark matter. The green squares show the nearest minimum in the dark matter to the left of the splashback radius (i.e. “the second caustic”). One can see that this is often not the steepest drop in the log-slope of the stars (i.e. the “edge” of the galaxy, as defined by the steepest drop in the stellar density log-slope, does not necessarily coincide with the second dark matter caustic). Five out of 10 Milky Way / M31 analogues have their steepest density log-slope between $0.5-0.6 R_{200,m}$, two are located closer to $0.3R_{200,m}$ and 3 above $0.7R_{200,m}$. We have previously shown that some of these discrepancies are due to the accretion histories of these galaxies (i.e. active or quiet). We will examine this point further in the next section, when we will discuss the origin of the shell features in the $v_r - D$ space.

5 FORMATION OF CAUSTICS

5.1 Dark matter and stars stripped from infalling dwarfs

We have so far established that the stars and dark matter stripped from dwarf galaxies get deposited in the halo, forming ‘shells’ in $v_r - D$ space. In particular, stars and dark matter piling up close to their apocentres cause radial overdensities, leading to features in log-slope of the density profile. In this Section, we examine how

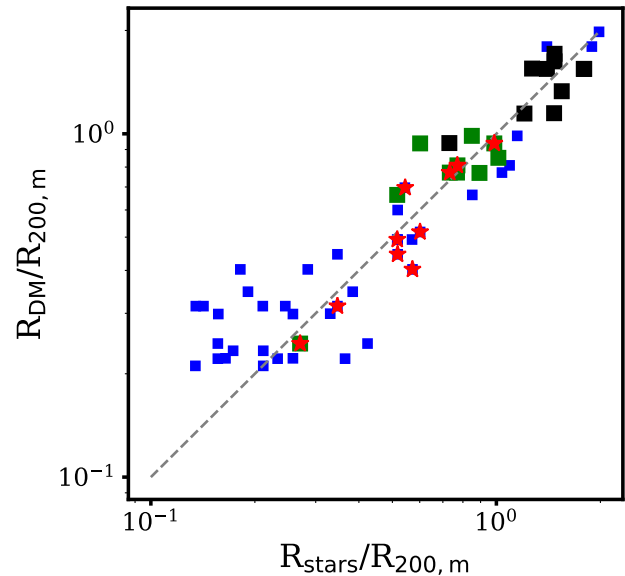


Figure 7. The minima in the log-slope of the density profile of the stars and the dark matter. For each minimum found in the log-slope of the stars, we find the nearest minimum in the log-slope of the dark matter density. The blue squares show all minima. The red stars show the steepest minima identified for each Milky Way / M31 analogue in the sample. The black squares show the closest stellar minima to the dark matter splashback radius. The green squares show the “second caustic” in the dark matter – the minimum closest to the splashback radius.

the stars and the dark matter stripped from dwarf galaxies infalling into the Milky Way / M31 analogues are distributed in the halo. We will focus on the particular example of a quiet galaxy, V1 0, which we have previously shown on the left panel of Fig. 6. For this analogue, we identify the biggest contributors to the stellar halo, both disrupted and surviving, and plot the histogram of the stripped particles’ locations within the halo. This is shown on the left of Fig. 8. Different contributors are identified with different colours, ordered by the stellar mass contributed to the halo. Note that this is not necessarily reflected by the peak stellar mass and that the greatest contributors of stars are not necessarily the greatest contributors of dark matter.

We see a number of interesting features. First, we are able to determine which dwarfs cause the ‘overdensities’, corresponding to particles piling up at the apocentres, and how these lead to the fluctuations in the log-slope of the stellar density (black solid line compared to black dotted line). Secondly, we see that the coincident minima in the log-slopes of the stars and the dark matter are not necessarily caused by the same dwarf galaxies. For example, the minimum in the stars at $\sim 0.8R_{200,m}$ is caused by the stars stripped from dwarf 837, whereas the corresponding feature in the dark matter seems to be due to some combination of 483, 577 and 837. We also see that each dwarf contributes substantial amounts of dark matter at each ‘peak’ (likely, subsequent apocentres of stripped particles as the dwarf sinks), with some increase in contribution towards the centre. At the same time, the stars are stripped in small amounts at the outskirts of the halo and substantially more towards the centre. Moreover, ‘peaks’ of stripped stellar and dark matter particles from the same dwarf galaxy do not appear to always align. This may be one of the reasons for the offsets observed between corresponding log-slope minima in the stars and the dark matter:

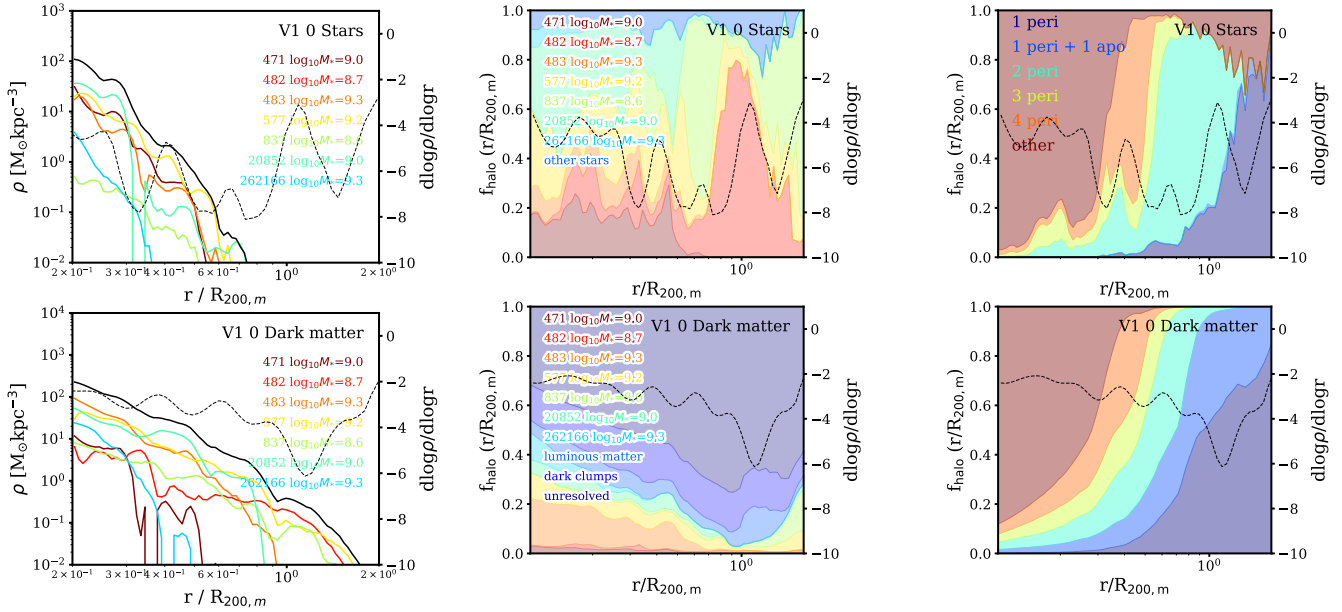


Figure 8. *Left:* density profiles of particles stripped from the biggest contributors to the stellar halo of Milky Way analogue **V1 0**. The peak stellar masses of each contributing dwarf are shown in the top right, together with their HBT+ identifying number. The black solid line is the combined density at each radius and the dotted line is the log-slope profile (with the scale shown on the right y-axis). *Middle:* the radial composition of the stellar and dark matter haloes at each radius. The contributions are split into the most important contributors to the stellar halo, other dwarfs, dark haloes, and the ‘smooth’ component. *Right:* The radial composition of the halo at each radius, split into the number of pericentres that the particles have undergone since infall. The steepest drop in the log-slope of the stellar density occurs at the boundary of the 2 and 3-pericentre material. The splashback radius of the dark matter is located roughly where the material has completed half of an orbit (1 pericentre after infall and one consequent apocentre).

overlapping contributions from various dwarfs and the differences in the stellar and dark matter stripping (Libeskind et al. 2011).

In the middle panel of Fig. 8, we show the radial composition of the stellar and dark matter haloes in cumulative form, focusing on the contributions from the main stellar contributors, but showing in addition the contribution from smaller luminous and dark haloes and the smooth component. For the stellar halo in particular, it is clear that our interpretation of the role of the top 4 mergers in creating the caustics in the log-slope density profile is correct. For the dark matter, the picture is somewhat more complex, as the four main stellar contributors account for no more than 15 per cent of the dark matter halo out to $R_{200,m}$; this figure primarily captures the radial contribution of each component rather than the overall density. However, one can see that of all components, it is the contributions of dwarfs 577 and 483 that show oscillatory behaviour that can be associated with variations in the log-slope. It is remarkable that objects that contribute no more than 10–20 per cent of the dark matter halo out to $R_{200,m}$ can cause such strong variations in the density slope, which are also observable in the stellar distribution.

5.2 Completed pericentres

It is tempting to associate the consecutive ‘peaks’ in the locations of particles of a given dwarf galaxy to the streams stripped off as the dwarf sinks to the centre of the host galaxy due to dynamical friction. As particles are primarily stripped near pericentre, in this section we explore how the number of pericentres completed by the particles in the halo relates to the particle spatial distribution, and thus to variations in the log-slope of the density profile (Diemer 2022).

5.2.1 Counting pericentres

We find the number of pericentres that a particle has completed by counting the number of times that its radial velocity, v_r , has changed sign. We also require that an apocentre count can only follow a pericentre and vice-versa. There are, however, some caveats to this method. Firstly, we are largely limited by the frequency of output times in our simulations, which decrease with decreasing redshift. If a particle has completed an orbit and the orbital time is shorter than the time interval between two simulation outputs, a pericentre cannot be counted. This is a major problem of this method. However, as we show in the following, the particles which make up the outer regions of the halo have long orbital time periods and would have completed typically no more than 4 full orbits during the dynamical time of the Milky Way analogue. These particles are immune to the limitation of infrequent simulation time outputs.

Another limitation is that subhaloes can interact with each other within a host galaxy, sometimes flipping the sign of v_r with respect of the Milky Way. We avoid this problem issue by requiring that a pericentre or an apocentre of an orbit be counted only if the change in the sign of v_r lasts longer than one simulation output. Again, this can undercount the number of pericentres or apocentres for orbits with short time periods, but has no effect on orbits with long orbital times which are of interest here.

5.2.2 Stellar and dark matter halo split by number of pericentres

On the right panels of Fig. 8, we show the radial contribution of particles with consecutive numbers of completed pericentres for the stars (top) and dark matter (bottom). It is remarkable to see the differences between the two. The stars have a distinctly clumpy

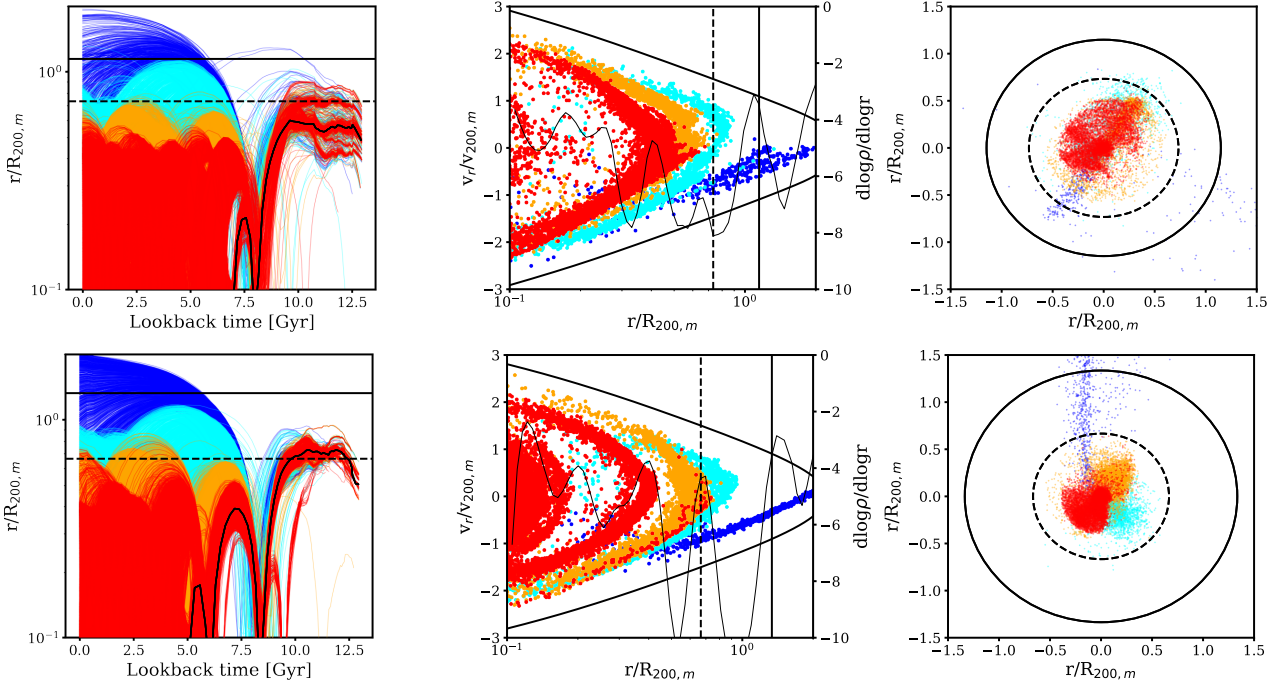


Figure 9. Examples of the stripping of massive dwarfs on more radial (top) and more tangential (bottom) initial orbits, leading to the formation of shell-like and umbrella-like features, respectively. *Left:* positions as a function of time of stars that have undergone 1 (blue), 2 (cyan), 3 (orange) and 4 (red) pericentres; the solid line tracks the orbit of the infalling dwarf galaxy. The dashed line is the location of the steepest drop in the log-slope of the stellar density profile. The black line is the splashback radius. The positions on the y-axis are in physical coordinates. *Center:* phase-space diagram showing the stars that have completed each number of pericentres. The thin black curve is the log-slope of the density profile. *Right:* x-y positions of the particles in the x-y coordinates of the simulation box.

distribution, while the dark matter resembles almost evenly spatially distributed ‘shells’ of matter on consecutive pericentres. In both cases, however, particles with more completed pericentres dominate at smaller radii and particles with fewer pericentres dominate at the outskirts.

A clear distinction between stars and dark matter in this case is the presence of dark matter particles that have had one pericentre and one apocentre (lighter blue). These particles effectively define the splashback radius of the halo and there are almost none visible in the stars. This likely reflects the differences in the build-up of the two types of haloes. Dark matter includes the smooth component as well as dark and luminous subhaloes which altogether dominate the outer halo (see centre of Fig. 8). The stellar halo, on the other hand, is dominated by the debris from a few past mergers in these regions, which have almost no stars with apocentres reaching $\sim R_{200,m}$ (left of Fig. 8).

The ‘edge’ of the galaxy, as defined by the steepest drop in the log-slope of the stellar density distribution, is coincident with the region where the three-pericentre material dominates, while across the two steepest log-slope drops, the 2-pericentre material is dominant overall. The latter could be connected to dwarfs 577 and 837 contributing to the stellar halo (see centre of Fig. 8).

5.3 Examples of past major mergers

We now examine in more detail the processes that lead to the formation of shells in the $v_r - D$ diagram. First, we identify dwarfs the which contributed the most stars to the stellar halo of the Milky Way/M31 analogue. We then follow the history of these objects –

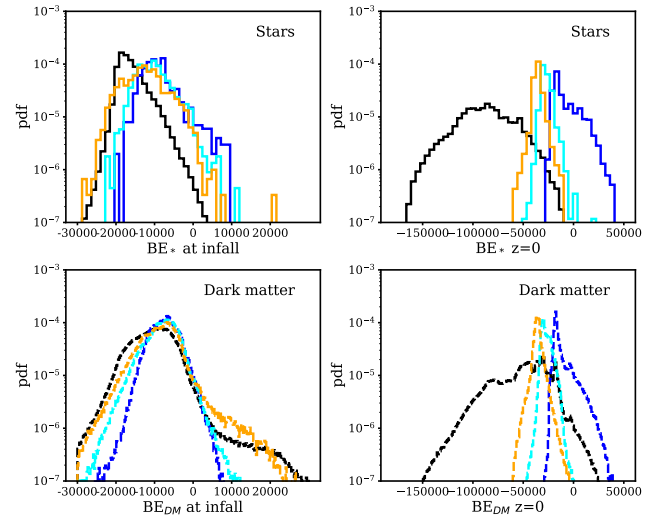


Figure 10. The binding energy of the star (top) and dark matter (bottom) particles of the merger shown in the top panel of Fig. 10. The binding energy at the time of infall is shown on the left and the binding energy at $z = 0$, with respect to the Milky Way analogue, is shown on the right. The blue, cyan and orange colours represent particles that have undergone 1, 2 and 3 pericentres, respectively. The black lines show all the particles that were bound to the dwarf at infall (i.e. when they crossed $R_{200,m}$).

their infall into the Milky Way / M31 analogues and the stripping of their stars and dark matter.

Figure 9 demonstrates the history of two dwarfs that merged

into two different Milky Way / M31 analogues. In the upper panel, the infalling dwarf enters the halo on a very radial orbit, reaches its first pericentre at ~ 8 Gyr and has one further apocentre before merging with the host halo. The orbital apocentre can be seen to be rapidly damped by the effects of dynamical friction (Amorisco 2017). The colours in this plot denote the number of pericentres that the particles have gone through by $z = 0$, with blue showing 1 pericentre and red 4 pericentres. We do not include particles with more pericentres in this figure.

Firstly, one can see that the material located in the outer stellar halo has been stripped primarily at the first pericentre of the dwarf’s orbit. From there, the stellar particles are dumped on a wide range of orbits, showing a spread in orbital energies that leads to some particles having fewer pericentres than others. Those with longer orbital times are the particles making up the outer regions of the stellar halo. In the middle panel of Fig. 9, it can be seen that the ‘shells’ in the $v_r - D$ diagram, corresponding to particles with varying numbers of pericentres coincide with the minima in the log-slope of the density. The particles that have only had one pericentre (the first pericentre of the merging dwarf) are ejected in some cases beyond the splashback radius of the halo (solid black line) - some can become unbound. In the $v_r - D$ diagram, these particles look as if they are being accreted onto the halo, with generally negative radial velocities, while in the X-Y diagram it can be seen that they form a kind of a ‘jet’ from the centre of the halo. These are akin to Gaia-Enceladus “arches” seen in the Toomre diagram (Koppelman et al. 2020; Naidu et al. 2021), which likely originate from stars on prograde orbits within the disk of the infalling dwarf or stars belonging to the dwarf’s extended stellar halo. These stellar particles, and their apocentres, could be the best stellar tracer of the splashback radius of the halo (provided the halo has not significantly grown since the merger). The particles which have undergone at least two pericentres, and were originally dumped with lower orbital energies, are the ones that define the steepest drop in the log-slope of the stars. These are clearly on bound orbits within the halo and define the stellar halo ‘edge’, as proposed by Deason et al. (2020).

We observe a similar behaviour in the merger shown in the lower panel of Fig. 9. In this case, however, the merger comes in on a more tangential orbit. The dwarf is able to complete two full orbits before effectively merging with the host halo. The increased circularity of the orbit is also evident in the $v_r - D$ diagram, where the shells of particles are clearly more circular, compared to the ‘sharper’ shells of a merger on a more radial orbit. The X-Y plot on the bottom right of Fig. 9 demonstrates a distinct ‘umbrella’ shape, characteristic of mergers with higher angular momentum (Martínez-Delgado et al. 2010). A ‘jet’ of one-pericentre stars is visible once again and extends out to beyond the splashback radius of the halo. Note that the spread in orbital phases means that the ‘jet’ bends over, making a loop. Since the particles spend more time near apocentre, the density is enhanced in the outer radii.

In Fig. 10 we show the binding energies of particles that have undergone 1, 2 and 3 pericentres within the Milky Way analogue. In the top panel, we show the binding energy with respect to the dwarf galaxy at the time of infall (left) and with respect to the host halo at $z = 0$ (right). We show corresponding properties for the dark matter at the bottom. It can be seen that the particles with successively smaller number of completed pericentres were less bound in the dwarf galaxy at infall. In the dark matter, one can see already a tail of unbound particles at infall, while the stellar component is to a large extent still bound. This confirms that the dark matter is stripped earlier and more effectively than the stars. At the same time, comparing the binding energy distributions within the Milky

Way analogue at $z = 0$, one can see that the binding energies of the stars and the dark matter with the same number of pericentres are remarkably similar. As the binding energy is, in effect, the total energy of the orbit, it best traces the apocentre of the orbit. This figure thus reinforces the idea that the orbits of stellar particles stripped from a dwarf follow the orbits of dark matter particles of the same energy and have similar phase-space features. This also suggests that semi-analytical dark matter particle tagging techniques can give faithful representations of the stellar distributions (Bullock & Johnston 2005; Gómez et al. 2013; Cooper et al. 2017).

5.4 The relation between past mergers and features in the log-slope of the halo density profile

We now examine in more detail the relation between particle apocentres and the “edge” of the stellar halo, defined here as the location of the steepest drop in the log-slope of the stars. On the left panel of Fig. 11, we display the merger histories of the 10 Milky Way / M31 analogues (identified with lines of different colours). The vertical location of each point represents the 99th percentile of the apocentres of stars stripped from each dwarf. The dashed line marks the location of the steepest caustic. The sizes of the points reflect the fraction of the halo that each dwarf contributes, while the colours reflect the stellar masses of each dwarf. In this figure we only include objects that contribute at least 1 percent of the accreted stellar halo mass. Several trends are visible. Firstly, the oldest mergers tend to have smaller particle apocentres, and so they do not typically define the “edge” of the stellar halo. We can also see that the oldest mergers are typically less massive and thus contribute a smaller fraction of the halo. More recent mergers, on the other hand, have stripped off particles that reach successively larger radii. In each case, we can identify the mergers which most likely define the galaxy “edge”. These are typically dwarfs that fall in later and are, on average, more massive than those that came in earlier. As such, the stellar halo “edge” is caused by the apocentre pile-ups of the stars stripped in the last big merger.

We now seek to establish the conditions that determine our ability to use stellar tracers to map dark matter. We have previously seen that log-slope features can be identified in both components at roughly similar locations; however the stripping of the dark matter is more efficient than that of the stars and thus the ability of the stars to trace the dark matter in the halo will depend on the efficiency of the stripping and the similarity of the velocity distributions of stars and dark matter in the infalling dwarf. In the middle panel of Fig. 11, we show the stellar mass of a dwarf, which is related to the stellar velocity dispersion, and the ratio of maximum apocentres of the stripped stellar and dark matter particles. It can be seen that dwarfs that have more stellar mass – and thus higher velocity dispersion – have stripped stars that follow the stripped dark matter orbits more closely. This relation shows scatter, which appears to be related to the time of the merger. For a given stellar mass, the stripped stars trace the dark matter better for early mergers. This suggests that tidal stripping may be more efficient early on in the history of the Milky Way and could, in part, be due to a lower concentration of the dwarfs at higher redshift.

Given the differences between the stripping of stellar and dark matter particles, it is interesting to ask if there is a relation between the edge of the stellar halo and the location of the splashback radius. On the right of Fig. 11, we show the ratio of “edges” of merger debris to the splashback radius as a function of $M_{200,m}$. The points are coloured by the fraction of total present-day mass within $R_{200,m}$ that was in place at the time of the merger (this includes the merg-

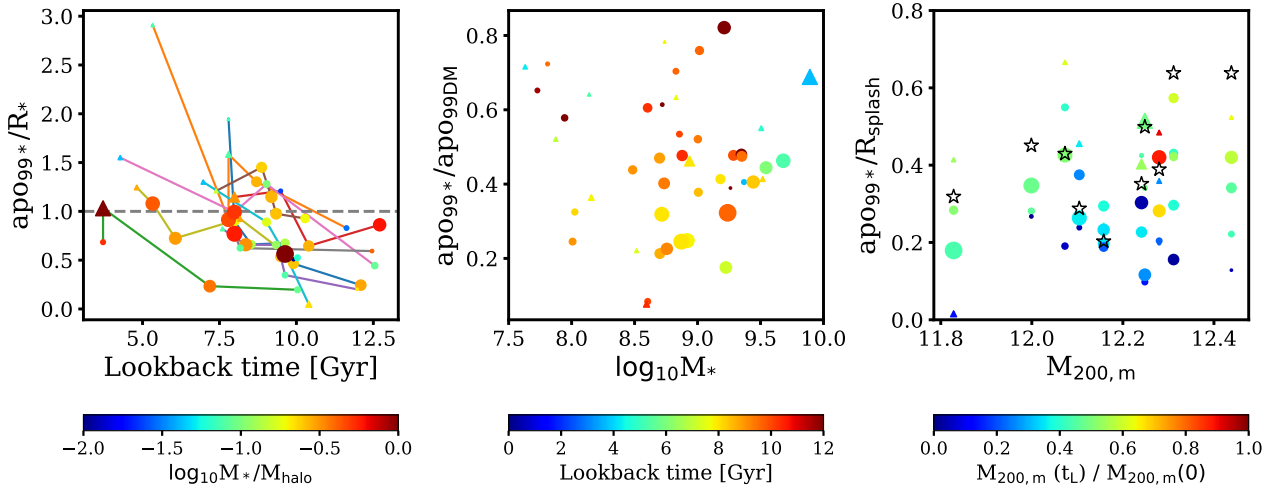


Figure 11. *Left:* merger histories of the 10 Milky Way / M31 analogues. The horizontal axis is the lookback time of the merger (defined as the first pericentre), while the vertical axis gives the location of the 99th percentile of the stellar particle apocentres of each merger event with respect to the location of the steepest drop in the log-slope of the stellar density profile, ap_{099}/R_* . The points are coloured by the ratio of the dwarf stellar mass to the present-day Milky Way / M31 analogue stellar halo mass. Circles show fully disrupted dwarfs and triangles show dwarfs that have not been disrupted. The size of the points reflects the fraction of the stellar halo contributed by each dwarf. Lines of different colours represent individual Milky Way / M31 analogues. *Middle:* ratio of the 99th percentiles of stellar and dark matter particle apocentres for dwarfs of each peak stellar mass. The points are coloured by the lookback time of the merger. *Right:* the location of particle apocentres with respect to the splashback radius, $ap_{099}/R_{\text{splash}}$, as a function of the total mass within $R_{200,m}$. The points are coloured by the fraction of the present-day $M_{200,m}$ that was already in place at the time of the merger. The star symbols show the location of the steepest drop in the log-slope of the stellar density.

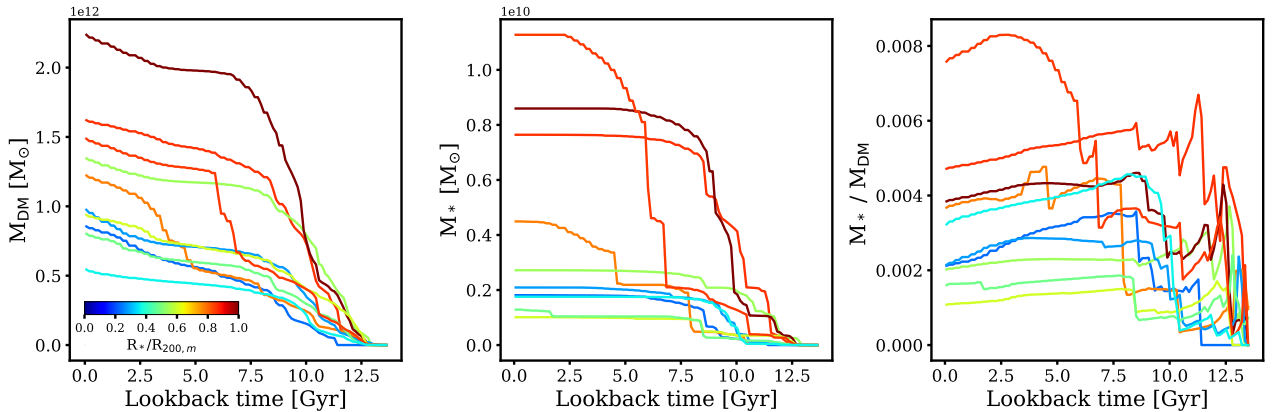


Figure 12. The assembly histories of the dark matter halo (left), the accreted stellar halo (centre) and the historical stellar mass-to-halo mass ratio of the Milky Way / M31 analogues (right). All are defined within $R_{200,m}$. The lines are coloured by the location of the steepest drop in the log-slope profile of the stars, $R_*/R_{200,m}$. Note that the low stellar-to-dark matter mass ratio does not imply a more embedded stellar halo.

ing dwarf). We can see that the more massive Milky Way / M31 analogues typically have galaxy “edges” that extend closer to the splashback radius, although there is some scatter. We note that the “edges” do not necessarily correspond to the furthest apocentres of the merger debris in some cases (see Fig. 7), though the stellar component beyond the edge is typically rather diffuse.

We find that the “edges” of our Milky Way analogues range between $0.2\text{--}0.65 R_{\text{splash}}$. We can see that the cases where the “edge” of the halo is more embedded also corresponds to the cases where the halo has not assembled more than 50 percent of its final mass at the time when the largest contributors to the stellar halo merged with the main galaxy. These objects correspond to our ‘active’ sample of Milky Way / M31 analogues. Overall, Fig. 11 suggests that there is no direct conversion between the galaxy “edge” and the splashback

radius; relating these two properties may require knowledge of the recent growth history of the dark matter halo. We expand on this feature of some of our Milky Way/M31 analogues in the next section.

5.5 What determines the “edge” of the galaxy?

We now explore the main factors behind the location of the steepest drop in the log-slope of the density profile of the stars relative to $R_{200,m}$. From past work on the splashback radius of the halo, some of the main factors were identified as the halo mass and the mass accretion rate of the halo, typically defined from a halo dynamical time of ~ 8.5 Gyr ago to the present day. While our analogue galaxies were selected to match the constraints for the Milky Way and M31, there is still a noticeable variety in stellar and dark matter

halo masses. In Fig. 12, we show the mass assembly histories of the dark matter halo (left) and the stellar halo (centre). The right panel shows the evolution of the stellar-to-dark matter halo mass ratio. The lines are coloured by the location of the galaxy ‘edge’, defined by the location of the steepest caustic.

From the left panel of Fig. 12, in agreement with the right panel of Fig. 11, it is clear that the more massive dark matter haloes typically have their stellar halo edge further out relative to $R_{200,m}$, whereas the less massive haloes have a stellar halo edge that is more embedded. This suggests that dark matter halo mass is an important driver of the location of the stellar halo edge. Nevertheless, we also see a number of outliers – for example, the fourth most massive halo has an edge at $\sim 0.5R_{200,m}$, while the fifth most massive has it at $0.7R_{200,m}$. Galaxies with bigger stellar haloes also tend to have a higher stellar mass, though it does not appear to be the case that the stellar mass alone can explain the location of the halo edge (middle panel of Fig. 12).

To further investigate the source of this diversity, we look at the historical stellar-to-dark matter halo mass relation (right panel of Fig. 12). We see that the more massive dark matter haloes also tend to have higher M_*/M_{DM} , as expected (Behroozi et al. 2013; Moster et al. 2013). If the total stellar mass to dark mass in the infalling dwarf is relatively high, this could result in more stars being stripped earlier on after infall, allowing stars to trace the stripped dark matter further out in the halo and simultaneously ‘pushing’ the stellar halo edge further out.

However, it does not appear to be the case that the smaller values of M_*/M_{DM} lead to more embedded stellar haloes. For example, the Milky Way / M31 analogue with the lowest M_*/M_{DM} has its stellar halo edge at $\sim 0.6R_{200,m}$, while a halo with $M_*/M_{\text{DM}} \approx 0.003$ has its edge at $\sim 0.3R_{200,m}$. However, there is one feature that distinguishes the ‘blue’ curves from the ‘green’: the rate of change of M_*/M_{DM} , whereby haloes with more embedded haloes have M_*/M_{DM} declining more steeply with time. From the middle panel of Fig. 12, it is clear that the stellar haloes are almost completely assembled ~ 8 Gyr ago. This suggests that the main driver of the change in M_*/M_{DM} is a faster dark matter assembly. The growth of the dark matter halo in the last few gigayears leads to the increased concentration of the stellar halo within the dark halo, although the total halo mass is also an important factor.

The Milky Way / M31 analogues where the “edge” is more concentrated relative to $R_{200,m}$ or the splashback radius belong to our ‘active’ sample. Looking at the stack of this sample on the right of Fig. 5, it is clear what causes this accelerated growth in the dark matter mass: these objects tend to have a massive satellite that deposits a large amount of the dark matter into the halo, but not so much in the stars. This is reminiscent of the Large Magellanic Cloud, which could have contributed a significant fraction of the total mass of the Milky Way, but has not experienced significant stripping of stars as it is likely on its first infall (Besla et al. 2010; Conroy et al. 2021; Petersen & Peñarrubia 2020; Garavito-Camargo et al. 2021).

6 OBSERVATIONAL PROSPECTS

In this section, we discuss the prospects for identifying the remnants of the past mergers that contribute to the stellar halo through their kinematic and chemical properties. We further explore whether halo ‘edges’ of external galaxies can be identified with deep photometry and connected to the underlying dark matter halo and its assembly history.

6.1 Chemo-kinematic properties of past mergers

In Fig. 13, we select 5 important mergers in the history of a quiet Milky Way analogue. These are identified with different colours and the symbol size corresponds to the fraction of stars they contribute to the stellar halo. It can be seen that these different dwarf galaxies are indistinguishable in the energy-angular momentum space at small radii, where most of the data are available (the right panel of Fig. 13 shows the typical galactocentric distance at each energy). Any significant deviations from the mean energy and angular momentum can only be seen in the outer regions of the halo, beyond ~ 100 kpc or so, where the stars have not yet phase-mixed. However, the contributing dwarfs have somewhat different metallicities. This suggests a way to distinguish past mergers. Moreover, a metallicity gradient can be seen, whereby the stars in the outer halo are more metal-poor than the stars in the inner halo. The stars which are more bound also tend to have lower metallicities, suggesting that the most bound stars come from the most ancient mergers. While the stars are significantly phase-mixed in the inner regions, making it difficult to distinguish different progenitors through their kinematics, the metallicities can differ sufficiently to tell the separate components apart. If the stellar ages are taken into account, one could use the redshift-dependent mass-metallicity relation to disentangle the different progenitors (see e.g. Monachesi et al. 2019).

Overall, our results suggest that detailed chemistry and, ideally, stellar ages are required to disentangle the origins of individual stars in the inner regions of the halo (see e.g. Naidu et al. 2020), while kinematics are sufficient to identify individual structures in the outer halo. Note, however, that our results also suggest that the stars stripped from the same dwarf can have prograde and retrograde motions and in that case one must employ additional information to avoid classifying these as separate structures (Simion et al. 2019; Kim et al. 2021; Amarante et al. 2022). These results are in agreement with the findings from the HESTIA simulations (Khoperskov et al. 2022), who show that the debris from a single merger occupies a wide area of $L_z - E$ space that overlaps with other mergers, but also has several overdensities in this space. The asymmetric and time-variable halo potential leads the location of the debris in the action-angle space to change over time. This work also found that enhanced star formation in the dwarf that is about to merge leads the ages of the most recently stripped stars to correspond to merger time. This feature may be used to recover the Milky Way’s assembly history.

6.2 The surface brightness of the stellar halo edge

We have so far shown that some of the most important mergers that define the ‘edge’ of the stellar halo of Milky Way-like galaxies leave the most kinematically distinct traces in the outskirts of haloes, beyond ~ 100 kpc. Aside from kinematics, we have shown that the stellar density profile also shows variations due to particle ‘pile-ups’ at apocentre, which are associated with the dark matter halo mass and assembly history.

What do the variations in the log-slope of the stellar density profile mean in terms of surface brightness? To compute the AB V-band magnitudes of the stellar particles in our simulations we use the FSPS software (Conroy et al. 2009; Conroy & Gunn 2010), where we adopt the Padova stellar isochrone library (Bertelli et al. 2008, 2009) and a Chabrier (2003) initial mass function. For each stellar particle, we provide its age and smoothed metallicity to the code. In the top panel of Fig. 14, we show the surface brightness profiles of our 10 Milky Way / M31 analogues, computed using

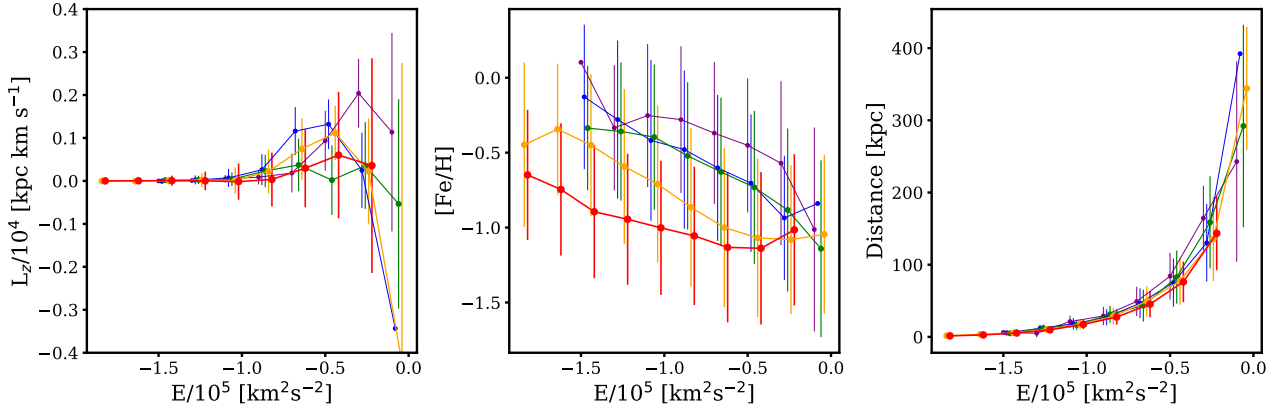


Figure 13. The properties of particles for the 5 most important contributors to the stellar halo of **V10** shown with different colours. The size of the points shows the fraction of the stellar halo made up by each dwarf. *Left:* angular momentum of the particles as a function of orbital energy. *Centre:* metallicity as a function of orbital energy, in solar units. *Right:* distance from the Milky Way / M31 analogue centre as a function of energy.

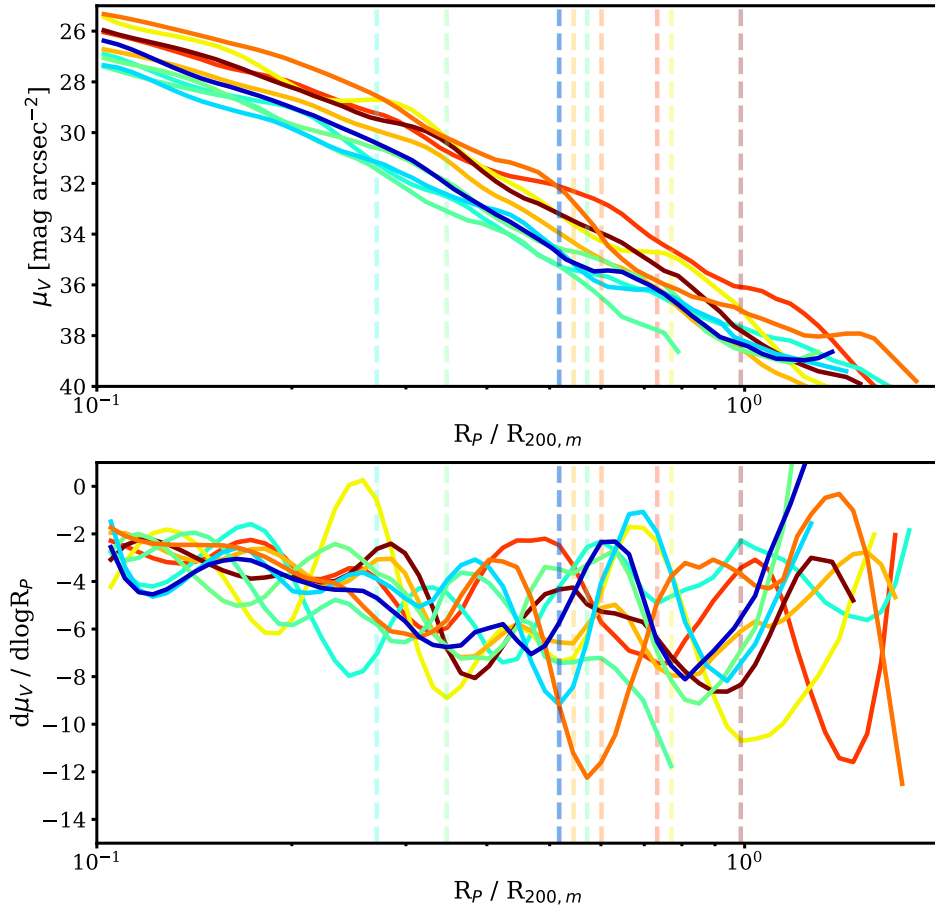


Figure 14. The stellar surface brightness profiles in the V-band (top) and the slope of the surface brightness (bottom) as a function of radius, normalized by $R_{200,m}$. Each Milky Way / M31 analogue is labeled with a unique colour, reflecting the mass of the dark halo (blue is lower mass, and red is higher mass). The vertical dashed lines mark the location of the steepest caustic in 3D.

an arbitrary projection. In order to avoid contributions from the closest galaxy (as our systems form a Local Group), we exclude all particles within $R_{200,m}$ of the companion halo. As for the 3D profiles, we compute the profiles in 75 radial bins and 11 angular bins, taking the median of the angular bins at each radius. We

smooth the profiles using the Savitzky-Golay filter (Savitzky & Golay 1964). Each analogue is identified with a unique colour. One can see clearly that the surface brightness profiles of the haloes are not smooth, but exhibit variations similar to those found by Deason

et al. (2020). These variations are substantially more pronounced in the computed surface brightness slope (bottom panel of Fig. 14).

The vertical dashed lines in Fig. 14 show the location of the steepest drop in the log-slope of the 3D stellar density profile. This is typically further than the nearest drop in the log-slope of the surface brightness, as expected from projection effects. While the location of the halo edge varies, as we have discussed previously, the typical location, $0.5\text{--}0.6 R_{200,m}$, occurs at a V-band surface brightness of between $31\text{--}36 \text{ mag arcsec}^{-2}$, marginally achievable with the Euclid Deep Survey (Laureijs et al. 2011), Hubble Ultra Deep Field (Beckwith et al. 2006) and 10-year Legacy Survey of Space and Time (Martin et al. 2022), albeit with typically smaller survey areas. Targeted low-surface brightness surveys, like Dragonfly Nearby Galaxies Survey (DNGS) are already achieving comparable levels of surface brightness (Abraham & van Dokkum 2014). An alternative is to stack images of Milky Way-mass galaxies (D’Souza et al. 2014; Wang et al. 2019), as has been done in the past in the search for splashback radius in galaxy clusters (More et al. 2016).

7 SUMMARY AND CONCLUSIONS

The Cold Dark Matter model implies hierarchical structure formation in our Universe, where smaller structures form first and accumulate to former larger ones. The model predicts the typical assembly histories, with scatter, for galaxies such as our own Milky Way. Since the presence of dark matter has been observed only indirectly, one has to rely on the visible baryonic component to infer the total matter content and the assembly history of galaxies like the Milky Way. The emergence of cosmological hydrodynamic simulations has allowed us to model the formation and evolution of galaxies within the Λ CDM paradigm. These simulations make predictions for how the stellar halo of the Milky Way has assembled through past accretion events and how this relates to the assembly of the dark matter halo. In particular, one can look for signatures in the stellar component that would reveal the properties of the dark matter. In this work we have examined the build-up of Milky Way-mass haloes in Local Group-like environments from the APOSTLE suite of simulations. We have examined both stellar and dark matter halo build-up through accretion. We find the following:

i) In the CDM paradigm of hierarchical structure formation, large dark matter haloes are built up through accumulation of smaller clumps (Frenk et al. 1988). By mass, subhaloes that have hosted stars make up 30–40 per cent of a galactic dark matter halo, with the ‘smooth’ halo component making up the majority of the mass (35–40 per cent). The smooth component is itself split into particles that are not in bound structures as well as those in haloes of mass below the resolution limit of our simulations (subhaloes $< 10^9 M_{\odot}$, where the power-law form of the CDM mass function breaks down.) The contributions of the dark and the luminous components are quite similar and it is their relative sizes that determine the degree to which the stars in the halo are able spatially to trace the dark matter (the stellar mass – halo mass relation).

ii) The accreted stellar halo of Milky Way-like galaxies is primarily built up from disrupted dwarfs (~ 85 per cent). Stars stripped from surviving dwarfs typically make up 10–15 per cent of the stellar halo. It is typically 5–6 dwarfs with peak stellar mass of $> 10^9 M_{\odot}$ that make up ~ 80 per cent of the stellar halo in Milky Way-mass galaxies; of those the majority are disrupted.

iii) We identify ‘active’ and ‘quiet’ Milky Way / M31 analogues in our sample of 10 galaxies, in equal numbers. The main distinction between the two is the relative contribution of surviving subhaloes and the distribution of their debris in the halo. This has to do with the order in which particles are stripped from dwarf galaxies – dark matter stripping occurs before stripping of stars due to the more extended spatial distribution of dark matter particles and their lower binding energies (Libeskind et al. 2011). We also find that the halo stars in ‘active’ galaxies are more centrally concentrated than in the quiet sample, which overall results in more embedded stellar haloes. Active galaxies also have a more significant dark matter contribution from disrupted dark haloes in the outer regions. Radial accretion and stripping time gradients suggest this is due to subhaloes that began to be stripped prior to crossing $R_{200,m}$ while in a group with larger haloes.

iv) The disruption of dwarf galaxies as they fall into the Milky Way leaves structural imprints on the phase-space distribution. On a $v_r - D$ diagram, this takes the form of shells of particles following similar orbits in both stars and dark matter. Structures seen in the stellar halo have corresponding structures in the dark matter, although in the latter case they are “smoothed out” due to the dominance of the smooth dark matter component, particularly beyond $0.1R_{200,m}$ (smaller radii are not better places to look for such structures due to increasingly phase-mixed material in those regions). If the smooth component is removed from the analysis, the $v_r - D$ structure of the dark matter halo in the outer regions follows closely that of the stars.

v) In agreement with Deason et al. (2020), we find that the log-slope of the stellar halo density has a prominent trough at $\sim 0.5 - 0.6R_{200,m}$, although the exact location varies, corresponding to apocentre pile-ups of particles that have completed two–three orbital pericentres since infall into the Milky Way / M31 analogues. However, in this work we have examined simulations with higher mass resolution than Deason et al. (2020). As such, we were able to detect additional features in the stellar and dark matter halo density profiles, located closer in. Overall, we have found that even out to the splashback radius, variations in the dark matter density profile have corresponding variations in the density profile of the stars.

vi) We examined the formation of the shells that lead to the formation of the ‘edge’ of the galaxy (i.e. the steepest drop in the log-slope profile of the stars). We found that typically one or two mergers deposit particles in the outer regions that lead to deviations of the halo density profile from smoothness. Contributions from several important mergers can also add up to enhance variations in the density profile. Since the stripping of the dark matter is more efficient and more continuous along an orbit than for the stars, the ‘peaks’ in the radius of stripped dark matter particles can be offset from those of the stars stripped from the same objects, leading to slight differences in the locations of the density log-slope minima. Additionally, the dark matter content at large radii, where we expect to see the stellar halo edge, is dominated by the smooth component which suppresses variations in the density profile of the dark matter compared to corresponding features in the stars.

vii) We found a common behaviour in mergers that have contributed the most to the stellar halo of Milky Way-like galaxies. In agreement with previous work, we found that these objects enter the halo on very radial orbits due to their large mass and the undergo dynamical friction. The log-slope features that are detected in the stellar halo

outskirts correspond to particles that were typically stripped at the first pericentre of the satellite's orbit. The wide range in particle binding energies, particularly in the most massive mergers, leads to a spread of particle apocentres and orbital phases. Particles which were less bound within the infalling dwarf galaxy end up on more energetic orbits within the Milky Way after they are stripped and, consequently, complete fewer orbits by the present day. Depending on the time of the merger, a 'jet' of 1-pericentre stellar particles can be seen extending from the halo centre and looping around. If the halo has not grown significantly after the merger, these particles roughly trace the splashback radius of the dark matter halo. The steepest trough in the log-slope of the stellar density is the result of apocentre pile-ups of particles that have completed 2-3 orbits, depending on the halo growth since the merger. However, if the halo growth is particularly fast after the merger, these relations can break down as the stellar halo is dominated by particles that have not completed a full orbit. Although we have not explicitly demonstrated the same features in the dark matter, we have shown that stellar and dark matter particles with the same number of completed pericentres have very similar distributions of binding energies within the Milky Way analogues.

viii) We have looked into the specific histories of the dark matter and stellar halo growth, and their relation, to establish the main drivers of the location of the halo 'edge'. We have found that a large halo mass, which often corresponds to a large mass in the stellar halo, leads to more extended haloes. This reflects the fact that these haloes experienced more massive major mergers that had higher stellar mass contributions, allowing the stars to trace the dark matter out to larger radii. At the same time, halo mass does not seem to be the only important factor. Since the stellar haloes often assembled earlier than the dark matter, the subsequent dark halo growth leads to increased concentration of the stellar halo within the dark halo. This is consistent with previous work exploring the halo splashback radius. In particular, we find stellar halo "edges" to be more embedded within the dark matter halo if the halo has recently accreted a massive satellite that contributes roughly 25 per cent of the dark halo mass, while its stars have generally not been affected by tidal forces.

ix) We have examined the possibility of uncovering the important mergers contributing to the build-up of the stellar halo. We have found that the debris from these past mergers has a metallicity gradient across the stellar halo, likely stemming from the metallicity gradient within the objects themselves. More massive mergers typically have particles with higher binding energies (lower orbital energies) within the stellar halo and thus contribute more particles at small radii (central ~ 20 kpc), making them more likely to be detected. At the same time, across all radii, there is a large spread in the metallicity distribution that may overlap with other contributors. We have also examined the distributions of the orbital energy and angular momentum that may help distinguish different mergers kinematically. We found that at small radii (below ~ 50 kpc) the orbits are rather similar, likely due to mixing in a turbulent time-varying gravitational potential; however, at large radii the particle orbits of stars from different progenitor dwarfs become increasingly distinct from each other. This is likely where the particles are still on the first or second pericentre of the orbit, moving still somewhat coherently since the time they were stripped (see, for example, the 'jet' features in Fig. 9).

x) We find that the 'edge' of the stellar halo in Milky Way-like

galaxies typically corresponds to a surface brightness of $31-36$ mag arcsec $^{-2}$. Reaching this surface brightness limit is marginally possible with existing, though coverage-limited, ultra deep photometric surveys, like DNGS (Abraham & van Dokkum 2014). Alternatively, one may stack multiple images of Milky Way-mass galaxies in search of the 'edge' feature (D'Souza et al. 2014; Wang et al. 2019).

In this work, we have examined the predictions of the Λ CDM model, together with the EAGLE model of galaxy formation for the assembly of the accreted stellar and dark matter halos of Milky Way / M31 analogues in Local Group-like environments. Some aspects of this work may be sensitive to the assumed galaxy formation physics. For example, the details of the stellar-halo mass relation may, to some extent, alter the ability of stripped stars to track the dark matter. This could also be affected by the sizes of the galaxies. We note, however, that the galaxy formation model we have employed has been shown to reproduce these galaxy scaling relations (Crain et al. 2015; Schaye et al. 2015; Campbell et al. 2017), with the largest uncertainties expected both above the Milky Way mass and in the regime of the classical dwarf galaxies, in which the observed relations are not well constrained. We also do not expect small changes in the halo mass threshold above which galaxy formation occurs to affect our results significantly, since it is the most massive galaxies that contribute the majority of stars in the outer halo.

One limitation of this work in the context of the direct comparison of simulated haloes to the Milky Way and M31 lies in the morphology, assembly history and mass of the stellar discs. APOSTLE halo pairs were selected to match the observational constraints on the separation of Milky Way and M31 and their total mass. This does not however guarantee comparable formation histories, only a similar present-day local environment. The main galaxies in APOSTLE are known to be less massive than the Milky Way and M31 (Fattahi et al. 2016), which leads to reduced disruption of substructure by the potential of the disk (Richings et al. 2020). We expect however, that this does not change our conclusions on the contribution of the most massive dwarfs to the stellar halo, as these objects quickly sink and merge with the host galaxy due to dynamical friction. In addition, the work of Kelly et al. (2022) investigated the properties of disks in APOSTLE high-resolution volumes (which we use here) in comparison to the same galaxies simulated with the AURIGA model (Grand et al. 2017) at the same mass resolution. These authors found that the discs of the main galaxies in APOSTLE were too thick, had a factor of ~ 2 larger disc scale length and lacked the spiral arm and bar structures seen in AURIGA simulations, while the latter also formed a factor of ~ 2.5 more stellar mass. The authors suggested that this stems from the difference in effective spatial resolution, which is higher in mesh-based codes compared to SPH codes. Previous works have also shown that the disc can bias the debris of satellites accreted on low-inclination orbits into the disc plane (Quinn et al. 1993; Read et al. 2008). This may imply that the orientation of the satellite debris is somewhat more isotropic in our simulations than in typical disc galaxies. Nevertheless, this is unlikely to affect our results regarding the origin of the 'stellar splashback'.

What is perhaps more concerning is the larger thickness of the discs of star-forming dwarf galaxies in APOSTLE compared to observations (Oman et al. 2017), because the higher velocity dispersion in the stellar disc may cause premature stripping of the stars and thus an enhancement of the mass of the stellar debris deposited in the outskirts of the Milky Way / M31 analogues. If this

does have a noticeable effect, we expect that the surface brightness profile features due to apocentre pile-ups will be more concentrated than suggested by our simulations. On the other hand, the stars defining the “stellar splashback” primarily come about from the extended stellar haloes of accreted massive dwarf galaxies, rather than their discs (see e.g. the origin of the 2-pericentre particles on the left of Fig. 9, or the binding energy distribution in Fig. 10), so as long as these dwarf halo stars exist we expect that the stellar halo “edge”, as defined by the steepest drop in the log-slope of the stellar density profile, will not change significantly. What may change is the surface brightness at which the features are observed. The work of Keller (2022) describes in detail how the numerical implementation of supernovae feedback in simulations can alter the morphology of dwarf galaxies, leading to brighter or fainter stellar haloes of Milky Way-mass galaxies.

We have shown that the stripping of dwarf galaxy stars leads to the formation of shells in phase space that traces similar shells in the dark matter distribution. It would be interesting to explore whether these features are affected by the nature of the dark matter. For example, warm dark matter leads to the suppression of the matter power spectrum on small scales, such that low-mass haloes and the fraction of the smooth component made up of unresolved haloes would not exist in our simulations, potentially leading to more distinctive caustic features in the dark matter, and perhaps also in the stars, if small subhaloes perturb streams of stripped particles in CDM (Lovell et al. 2020).

Self-interacting dark matter (SIDM) may also result in a different phase-space picture. Firstly, dark matter haloes may suffer enhanced disruption due to ‘dark ram pressure’ stripping from the host galaxy halo (Spergel & Steinhardt 2000; Sirks et al. 2022). In some SIDM models cores form in dark matter haloes. Core formation is also expected in CDM galaxy formation models in which baryonic feedback is sufficiently impulsive Benítez-Llambay et al. (2019). It has been shown that tidal stripping is more efficient in haloes with cores, enhancing subhalo disruption and producing wider stellar and dark matter streams (Errani et al. 2015). This would lead to fuzzier streams of stripped particles and smoother halo density profiles, in which changes in the smoothly declining density slope are less easily identifiable.

ACKNOWLEDGEMENTS

AD and CSF are supported by the Science and Technology Facilities Council (STFC) [grant number ST/F001166/1, ST/I00162X/1, ST/P000541/1]. AD is supported by a Royal Society University Research Fellowship. CSF acknowledges a European Research Council (ERC) Advanced Investigator grant DMIDAS (GA 786910). This work used the DiRAC Data Centric system at Durham University, operated by the ICC on behalf of the STFC DiRAC HPC Facility (www.dirac.ac.uk). This equipment was funded by BIS National E-infrastructure capital grant ST/K00042X/1, STFC capital grant ST/H008519/1, and STFC DiRAC Operations grant ST/K003267/1 and Durham University. DiRAC is part of the National E-Infrastructure.

DATA AVAILABILITY

The data analysed in this article can be made available upon reasonable request to the corresponding author.

REFERENCES

- Abraham R. G., van Dokkum P. G., 2014, *PASP*, **126**, 55
- Adhikari S., Dalal N., Chamberlain R. T., 2014, *J. Cosmology Astropart. Phys.*, **2014**, 019
- Amarante J. A. S., Debattista V. P., Beraldo e Silva L., Laporte C. F. P., Deg N., 2022, arXiv e-prints, p. arXiv:2204.12187
- Amorisco N. C., 2017, *MNRAS*, **464**, 2882
- Beckwith S. V. W., et al., 2006, *AJ*, **132**, 1729
- Behroozi P. S., Wechsler R. H., Conroy C., 2013, *ApJ*, **770**, 57
- Belokurov V., Erkal D., Evans N. W., Koposov S. E., Deason A. J., 2018, *MNRAS*, **478**, 611
- Belokurov V., Sanders J. L., Fattahi A., Smith M. C., Deason A. J., Evans N. W., Grand R. J. J., 2020, *MNRAS*, **494**, 3880
- Benítez-Llambay A., Frenk C., 2020, *MNRAS*, **498**, 4887
- Benítez-Llambay A., Frenk C. S., Ludlow A. D., Navarro J. F., 2019, *MNRAS*, **488**, 2387
- Benson A. J., Frenk C. S., Lacey C. G., Baugh C. M., Cole S., 2002, *MNRAS*, **333**, 177
- Benson A. J., Lacey C. G., Frenk C. S., Baugh C. M., Cole S., 2004, *MNRAS*, **351**, 1215
- Bernard E. J., et al., 2016, *MNRAS*, **463**, 1759
- Bertelli G., Girardi L., Marigo P., Nasi E., 2008, *A&A*, **484**, 815
- Bertelli G., Nasi E., Girardi L., Marigo P., 2009, *A&A*, **508**, 355
- Bertschinger E., 1985, *ApJS*, **58**, 39
- Besla G., Kallivayalil N., Hernquist L., van der Marel R. P., Cox T. J., Kereš D., 2010, *ApJ*, **721**, L97
- Bonaca A., et al., 2021, *ApJ*, **909**, L26
- Booth C. M., Schaye J., 2009, *MNRAS*, **398**, 53
- Bullock J. S., Johnston K. V., 2005, *ApJ*, **635**, 931
- Bullock J. S., Kravtsov A. V., Weinberg D. H., 2000, *ApJ*, **539**, 517
- Campbell D. J. R., et al., 2017, *MNRAS*, **469**, 2335
- Chabrier G., 2003, *PASP*, **115**, 763
- Chapman S. C., Ibata R., Lewis G. F., Ferguson A. M. N., Irwin M., McConnachie A., Tanvir N., 2006, *ApJ*, **653**, 255
- Conroy C., Gunn J. E., 2010, *ApJ*, **712**, 833
- Conroy C., Gunn J. E., White M., 2009, *ApJ*, **699**, 486
- Conroy C., Naidu R. P., Garavito-Camargo N., Besla G., Zaritsky D., Bonaca A., Johnson B. D., 2021, *Nature*, **592**, 534
- Cooper A. P., et al., 2010, *MNRAS*, **406**, 744
- Cooper A. P., et al., 2011, *ApJ*, **743**, L21
- Cooper A. P., Cole S., Frenk C. S., Le Bret T., Pontzen A., 2017, *MNRAS*, **469**, 1691
- Crain R. A., et al., 2015, *MNRAS*, **450**, 1937
- D’Souza R., Kauffman G., Wang J., Vegetti S., 2014, *MNRAS*, **443**, 1433
- Dalla Vecchia C., Schaye J., 2012, *MNRAS*, **426**, 140
- Davidge T. J., Pritchett C. J., 1990, *AJ*, **100**, 102
- Davis M., Efstathiou G., Frenk C. S., White S. D. M., 1985, *ApJ*, **292**, 371
- De Lucia G., Helmi A., 2008, *MNRAS*, **391**, 14
- Deason A. J., Belokurov V., Evans N. W., Johnston K. V., 2013, *ApJ*, **763**, 113
- Deason A. J., Mao Y.-Y., Wechsler R. H., 2016, *ApJ*, **821**, 5
- Deason A. J., Fattahi A., Frenk C. S., Grand R. J. J., Oman K. A., Garrison-Kimmel S., Simpson C. M., Navarro J. F., 2020, *MNRAS*, **496**, 3929
- Diemer B., 2022, *MNRAS*,
- Diemer B., Kravtsov A. V., 2014, *ApJ*, **789**, 1
- Diemer B., Mansfield P., Kravtsov A. V., More S., 2017, *ApJ*, **843**, 140
- Durrell P. R., Sarajedini A., Chandar R., 2010, *ApJ*, **718**, 1118
- Efstathiou G., 1992, *MNRAS*, **256**, 43P
- Eggen O. J., Lynden-Bell D., Sandage A. R., 1962, *ApJ*, **136**, 748
- Elias L. M., Sales L. V., Creasey P., Cooper M. C., Bullock J. S., Rich R. M., Hernquist L., 2018, *MNRAS*, **479**, 4004
- Errani R., Penarrubia J., Tormen G., 2015, *MNRAS*, **449**, L46
- Fattahi A., et al., 2016, *MNRAS*, **457**, 844
- Fattahi A., et al., 2020, *MNRAS*, **497**, 4459
- Fillmore J. A., Goldreich P., 1984, *ApJ*, **281**, 1
- Font A. S., McCarthy I. G., Crain R. A., Theuns T., Schaye J., Wiersma R. P. C., Dalla Vecchia C., 2011, *MNRAS*, **416**, 2802

- Font A. S., et al., 2020, *MNRAS*, **498**, 1765
- Frenk C. S., White S. D. M., Efstathiou G., Davis M., 1985, *Nature*, **317**, 595
- Frenk C. S., White S. D. M., Davis M., Efstathiou G., 1988, *ApJ*, **327**, 507
- Gaia Collaboration et al., 2018, *A&A*, **616**, A12
- Gaia Collaboration et al., 2021, *A&A*, **649**, A1
- Garavito-Camargo N., Besla G., Laporte C. F. P., Price-Whelan A. M., Cunningham E. C., Johnston K. V., Weinberg M., Gómez F. A., 2021, *ApJ*, **919**, 109
- Garrison-Kimmel S., Boylan-Kolchin M., Bullock J. S., Lee K., 2014, *MNRAS*, **438**, 2578
- Genina A., Frenk C. S., Benítez-Llambay A. r., Cole S., Navarro J. F., Oman K. A., Fattahi A., 2019, *MNRAS*, **488**, 2312
- Gómez F. A., Helmi A., 2010, *MNRAS*, **401**, 2285
- Gómez F. A., Helmi A., Cooper A. P., Frenk C. S., Navarro J. F., White S. D. M., 2013, *MNRAS*, **436**, 3602
- Gómez F. A., et al., 2017, *MNRAS*, **472**, 3722
- Grand R. J. J., et al., 2017, *MNRAS*, **467**, 179
- Gunn J. E., Gott J. Richard I., 1972, *ApJ*, **176**, 1
- Haardt F., Madau P., 2012, *ApJ*, **746**, 125
- Han J., Cole S., Frenk C. S., Benitez-Llambay A., Helly J., 2018, *MNRAS*, **474**, 604
- Harmsen B., Monachesi A., Bell E. F., de Jong R. S., Bailin J., Radburn-Smith D. J., Holwerda B. W., 2017, *MNRAS*, **466**, 1491
- Harris G. L. H., Harris W. E., 2000, *AJ*, **120**, 2423
- Helmi A., White S. D. M., 1999, *MNRAS*, **307**, 495
- Helmi A., de Zeeuw P. T., 2000, *MNRAS*, **319**, 657
- Helmi A., Babusiaux C., Koppelman H. H., Massari D., Veljanoski J., Brown A. G. A., 2018, *Nature*, **563**, 85
- Herzog-Arbeitman J., Lisanti M., Madau P., Necib L., 2018, *Phys. Rev. Lett.*, **120**, 041102
- Hopkins P. F., 2013, *MNRAS*, **428**, 2840
- Ibata R. A., Gilmore G., Irwin M. J., 1994, *Nature*, **370**, 194
- Ibata R. A., Gilmore G., Irwin M. J., 1995, *MNRAS*, **277**, 781
- Ibata R., Martin N. F., Irwin M., Chapman S., Ferguson A. M. N., Lewis G. F., McConnachie A. W., 2007a, *ApJ*, **671**, 1591
- Ibata R., Martin N. F., Irwin M., Chapman S., Ferguson A. M. N., Lewis G. F., McConnachie A. W., 2007b, *ApJ*, **671**, 1591
- Johnston K. V., Bullock J. S., Sharma S., Font A., Robertson B. E., Leitner S. N., 2008, *ApJ*, **689**, 936
- Keller B. W., 2022, *ApJ*, **939**, 4
- Kelly A. J., Jenkins A., Deason A., Fattahi A., Grand R. J. J., Pakmor R., Springel V., Frenk C. S., 2022, *MNRAS*, **514**, 3113
- Kennicutt Robert C. J., 1998, *ApJ*, **498**, 541
- Khoperskov S., et al., 2022, arXiv e-prints, p. arXiv:2206.04522
- Kim Y. K., Lee Y. S., Beers T. C., Koo J.-R., 2021, *ApJ*, **911**, L21
- Komatsu E., et al., 2011, *ApJS*, **192**, 18
- Koppelman H. H., Bos R. O. Y., Helmi A., 2020, *A&A*, **642**, L18
- Kruijssen J. M. D., Pfeffer J. L., Reina-Campos M., Crain R. A., Bastian N., 2019, *MNRAS*, **486**, 3180
- Lancaster L., Belokurov V., Evans N. W., 2019, *MNRAS*, **484**, 2556
- Laureijs R., et al., 2011, arXiv e-prints, p. arXiv:1110.3193
- Libeskind N. I., Knebe A., Hoffman Y., Gottlöber S., Yepes G., 2011, *MNRAS*, **418**, 336
- Licquia T. C., Newman J. A., 2015, *ApJ*, **806**, 96
- Lovell M. R., Hellwing W., Ludlow A., Zavala J., Robertson A., Fattahi A., Frenk C. S., Hardwick J., 2020, *MNRAS*, **498**, 702
- Majewski S. R., Skrutskie M. F., Weinberg M. D., Ostheimer J. C., 2003, *ApJ*, **599**, 1082
- Malhan K., Ibata R. A., 2018, *MNRAS*, **477**, 4063
- Malhan K., et al., 2022, *ApJ*, **926**, 107
- Mansfield P., Kravtsov A. V., Diemer B., 2017, *ApJ*, **841**, 34
- Martin G., et al., 2022, *MNRAS*, **513**, 1459
- Martínez-Delgado D., et al., 2010, *AJ*, **140**, 962
- Martínez-Delgado D., et al., 2021, arXiv e-prints, p. arXiv:2104.06071
- Mateu C., Read J. I., Kawata D., 2018, *MNRAS*, **474**, 4112
- McConnachie A. W., et al., 2009, *Nature*, **461**, 66
- Minniti D., Zijlstra A. A., 1996, *ApJ*, **467**, L13
- Minniti D., Zijlstra A. A., Alonso M. V., 1999, *AJ*, **117**, 881
- Monachesi A., et al., 2013, *ApJ*, **766**, 106
- Monachesi A., et al., 2019, *MNRAS*, **485**, 2589
- More S., et al., 2016, *ApJ*, **825**, 39
- Moster B. P., Naab T., White S. D. M., 2013, *MNRAS*, **428**, 3121
- Mould J., Kristian J., 1986, *ApJ*, **305**, 591
- Naidu R. P., Conroy C., Bonaca A., Johnson B. D., Ting Y.-S., Caldwell N., Zaritsky D., Cargile P. A., 2020, *ApJ*, **901**, 48
- Naidu R. P., et al., 2021, *ApJ*, **923**, 92
- Necib L., Lisanti M., Belokurov V., 2019, *ApJ*, **874**, 3
- O'Hare C. A. J., Evans N. W., McCabe C., Myeong G., Belokurov V., 2020, *Phys. Rev. D*, **101**, 023006
- Odenkirchen M., et al., 2001, *ApJ*, **548**, L165
- Oman K. A., Marasco A., Navarro J. F., Frenk C. S., Schaye J., Benítez-Llambay A., 2017, preprint, (arXiv:1706.07478)
- Perek L., 1951, Bulletin of the Astronomical Institutes of Czechoslovakia, **2**, 57
- Petersen M. S., Peñarrubia J., 2020, *MNRAS*, **494**, L11
- Piatti A. E., Carballo-Bello J. A., 2020, *A&A*, **637**, L2
- Pillepich A., et al., 2014, *MNRAS*, **444**, 237
- Pritchett C. J., van den Bergh S., 1987, *ApJ*, **316**, 517
- Quinn P. J., Hernquist L., Fullagar D. P., 1993, *ApJ*, **403**, 74
- Quinn T., Katz N., Efstathiou G., 1996, *MNRAS*, **278**, L49
- Read J. I., Lake G., Agertz O., Debattista V. P., 2008, *MNRAS*, **389**, 1041
- Richings J., et al., 2020, *MNRAS*, **492**, 5780
- Roman N. G., 1954, *AJ*, **59**, 307
- Rosas-Guevara Y. M., et al., 2015, *MNRAS*, **454**, 1038
- Santistevan I. B., Wetzel A., El-Badry K., Bland-Hawthorn J., Boylan-Kolchin M., Bailin J., Faucher-Giguère C.-A., Benincasa S., 2020, *MNRAS*, **497**, 747
- Sarajedini A., Barker M. K., Geisler D., Harding P., Schommer R., 2006, *AJ*, **132**, 1361
- Savitzky A., Golay M. J. E., 1964, Analytical Chemistry, **36**, 1627
- Sawala T., et al., 2016, *MNRAS*, **457**, 1931
- Schaller M., Dalla Vecchia C., Schaye J., Bower R. G., Theuns T., Crain R. A., Furlong M., McCarthy I. G., 2015, *MNRAS*, **454**, 2277
- Schaye J., 2004, *ApJ*, **609**, 667
- Schaye J., Dalla Vecchia C., 2008, *MNRAS*, **383**, 1210
- Schaye J., et al., 2015, *MNRAS*, **446**, 521
- Schmidt M., 1959, *ApJ*, **129**, 243
- Searle L., Zinn R., 1978, *ApJ*, **225**, 357
- Shipp N., et al., 2018, *ApJ*, **862**, 114
- Simion I. T., Belokurov V., Kopusov S. E., 2019, *MNRAS*, **482**, 921
- Simpson C. M., et al., 2019, *MNRAS*, **490**, L32
- Sirks E. L., Oman K. A., Robertson A., Massey R., Frenk C., 2022, *MNRAS*, **511**, 5927
- Spergel D. N., Steinhardt P. J., 2000, *Physical Review Letters*, **84**, 3760
- Springel V., 2005, *MNRAS*, **364**, 1105
- Starkman N., Bovy J., Webb J. J., 2020, *MNRAS*, **493**, 4978
- Sugiura H., Nishimichi T., Rasera Y., Taruya A., 2020, *MNRAS*, **493**, 2765
- Thou A. A., Weinberg D. H., 1996, *ApJ*, **465**, 608
- Tissera P. B., Scannapieco C., 2014, *MNRAS*, **445**, L21
- Vogelsberger M., White S. D. M., 2011, *MNRAS*, **413**, 1419
- Vogelsberger M., White S. D. M., Mohayaee R., Springel V., 2009, *MNRAS*, **400**, 2174
- Wang J., et al., 2011, *MNRAS*, **413**, 1373
- Wang W., et al., 2019, *MNRAS*, **487**, 1580
- White S. D. M., Rees M. J., 1978, *MNRAS*, **183**, 341
- Wiersma R. P. C., Schaye J., Smith B. D., 2009a, *MNRAS*, **393**, 99
- Wiersma R. P. C., Schaye J., Theuns T., Dalla Vecchia C., Tornatore L., 2009b, *MNRAS*, **399**, 574
- Yu S., et al., 2020, *MNRAS*, **494**, 1539
- Zavala J., Okamoto T., Frenk C. S., 2008, *MNRAS*, **387**, 364
- Zolotov A., Willman B., Brooks A. M., Governato F., Brook C. B., Hogg D. W., Quinn T., Stinson G., 2009, *ApJ*, **702**, 1058
- van den Bosch F. C., Ogiya G., 2018, *MNRAS*, **475**, 4066

This paper has been typeset from a $\text{\TeX}/\text{\LaTeX}$ file prepared by the author.